

A kinematical study of the launching region of the blueshifted HH 46/47 outflow with SINFONI K-band observations[★]

M. Birney¹, C. Dougados², E. T. Whelan¹, B. Nisini³, S. Cabrit⁴ and Y. Zhang⁵.

¹ Department of Experimental Physics, Maynooth University, Maynooth, Co. Kildare, Ireland
e-mail: matthew.birney@mu.ie

² Univ. Grenoble Alpes, CNRS, IPAG, 38000 Grenoble, France

³ INAF – Osservatorio Astronomico di Roma, Via di Frascati 3300074, Monte Porzio Catone, Italy

⁴ PSL University, Sorbonne Université, Observatoire de Paris, LERMA, CNRS UMR 8112, 75014 Paris, France

⁵ Department of Astronomy, Shanghai Jiao Tong University, 800 Dongchuan Rd., Minhang, Shanghai 200240, China

Received –; accepted –

ABSTRACT

Context. Studying outflows is important as they may significantly contribute to angular momentum removal from the star/disk system, affecting disk evolution and planet formation.

Aims. To investigate the different outflow components; the collimated jet, wide-angled molecular outflow, and outflow cavity, of the Class I HH 46/47 outflow system. We focus on their kinematics.

Methods. We present Near Infrared (NIR) K-band integral field observations of the blue-shifted HH 46/47 outflow base obtained using VLT/SINFONI with an angular resolution of 0''.81. Our analysis focuses on [Fe II], H₂ 1–0 S(1), and Br-γ emission. We employ a wavelength recalibration technique based on OH telluric lines to probe the kinematics of the wide-angled flow with an accuracy of ~ 1 km s⁻¹ - 3 km s⁻¹.

Results. A velocity gradient of ~ 10 km s⁻¹ transverse to the outflow direction is confirmed in the wide-angled H₂ outflow cavity. The H₂ cavity peaks at radial velocities of ~ -15 km s⁻¹ to -30 km s⁻¹, and the atomic jet at $v_{\text{rad}} \sim -210$ km s⁻¹. The outflow exhibits a layered structure; the high-velocity [Fe II] and Br-γ jet is surrounded by a wide-angled H₂ outflow cavity, which is in turn nested within the continuum emission and CO molecular outflow. The continuum emission and H₂ outflow cavity are asymmetric with respect to the jet axis.

Conclusions. We propose that the origin of the asymmetries and the velocity gradient detected in the wide-angled H₂ cavity, is due to a wide-angled outflow or successive jet bowshocks expanding into an inhomogeneous ambient medium, or the presence of a secondary outflow. We eliminate outflow rotation as an exclusive origin of this velocity gradient due to large specific angular momenta values, $J(r) \approx 3000 - 4000$ km s⁻¹ au calculated from 1'' to 2'' along the outflow. The observations reveal the complexities inherent in outflow systems, and the risk of attributing transverse velocity gradients solely to rotation.

Key words. Herbig-Haro objects – ISM: individual objects (HH 46, HH 47) – ISM: jets and outflows – Stars: formation – Stars: winds, outflows – Stars: jets

1. Introduction

Outflows (jets and winds) from young stellar objects (YSOs) are ubiquitous, but their origin is a major open question in star formation (Frank et al. 2014; Pascucci et al. 2023). They are launched very early in the star formation process perpendicularly to the accretion disk surrounding the YSO, and can persist for several million years (Whelan 2014). Ejection in YSOs is intrinsically linked with accretion and the outflows interact with the surrounding envelope of quiescent material creating shocked regions (Hartigan 2003; Arce et al. 2007). Studying YSO outflows is important as they may significantly contribute to the angular momentum removal from the star/disk system, which is an unsolved dilemma in star formation (Pudritz & Ray 2019). Angular momentum transport plays a central role in the star formation process as the initial angular momentum present in dense star forming cores needs to be reduced by several orders of magnitude in order to permit a star or a multiple star system to form (Belloche 2013). Outflows also influence disk evolution

and likely affect planet formation and migration as they may interact with the planet forming regions of the disk (Pascucci et al. 2023).

Observing protostars is essential to gain insights on the most active period of accretion and ejection from the forming star and Class 0/I low mass sources have been much studied to date (Ray & Ferreira 2021). However, protostars are challenging to observe due to their heavily embedded nature. Their dusty and gaseous envelopes cause strong extinction, making it difficult to probe the inner regions of the disks where accretion occurs and where the earliest instances of planet formation are beginning. We can however learn about the ejection, and indirectly the inner disk properties, of these YSOs by studying their powerful outflows, once we select the most suitable tracers. Protostellar outflows from Class 0/I YSOs consist of high-velocity ($v \sim 100$ km s⁻¹ - 400 km s⁻¹), collimated jets launched from the innermost region of the disks, lower velocity ($v \sim 1$ km s⁻¹ - 30 km s⁻¹), wide-angled winds launched from larger disk radii (Frank et al. 2014; Pascucci et al. 2023) and entrained material from the surrounding envelope (Arce et al. 2013). Lower-velocity, wider outflow components surrounding the bases of class I jets were first

[★] Based on observations collected with the VLT operated by the European Southern Observatory under ESO program ID 0102.C-0615(A).

discovered by Davis (2002) using NIR narrow-band H₂ imaging. Cavities, which are defined as hollow, low-density regions created by the outflow, surrounding atomic jets are well documented phenomena (Habel et al. 2021), and Class I protostars are regularly seen with such cavities. The origin of these outflow cavities is currently debated. They may be directly or partly tracing intrinsic wide-angled disk winds originating from the disk surface (de Valon et al. 2022; López-Vázquez et al. 2024). They may be tracing an interaction region between some kind of wide-angled disk wind, either by magnetic (MHD) processes or thermal (photo-evaporative) processes, and the surrounding medium, be it static or an infalling envelope. They may also be produced by the stacking of successive jet bowshocks from a collimated, variable inner jet propagating into a density-stratified surrounding medium (Rabenanahary et al. 2022).

MHD (magnetohydrodynamic) processes in the rotating star-disk system, where magnetic field lines anchored in the accretion disk magneto-centrifugally launch material from the disk plane, are theorised to give rise to outflows (Ray & Ferreira 2021). Current models predict that MHD outflows emanate from a range of disk radii (the Disk wind model) or from a single narrow radial region (the X-wind model) (Ferreira 1997; Bai et al. 2016). In the disk wind model (Pudritz & Norman 1983; Konigl & Pudritz 2000; Pudritz et al. 2007), the high-velocity, collimated jet component is launched from the innermost regions of the disk, whilst the launching region of the lower-velocity, wide-angled outflow component is more radially extended along the disk and distributed over a larger range of disk radii. This is significant for both disk evolution and later, planet formation as wide-angled winds may affect these substantially. An alternative model for launching an outflow magneto-centrifugally is the X-wind model (Shu et al. 2000). In this model, the outflow is launched from a narrow radial region at the interface region between the inner disk edge and the stellar magnetosphere, the so called co-rotation radius. High-velocity, collimated jets and slower moving, wide-angled winds are also predicted with this model (Shang et al. 2020), however in contrast with the disk wind model, the wide-angled wind component in the X-wind model flows at much higher velocities as all of the magnetic outflow streamlines originate at the same disk radius.

Disk wind models predict a greater fraction of angular momentum removal from the star disk system as the outflow driving region extends further radially along the disk from the driving source, and specific angular momentum increases with disk radii (Anderson et al. 2003; Ferreira et al. 2006; Pudritz & Ray 2019; Lee et al. 2021). Therefore, measurements of outflow rotation which lead to estimates of specific angular momentum are critical for constraining the two MHD models and to date have tended to support the disk wind model (Coffey 2017). Wide-angled winds can offer information about angular momentum transport. As we can more readily spatially resolve the lateral component of these wide-angled winds, it is more promptly achievable to perform outflow rotation measurements (Tabone et al. 2017; Zhang et al. 2018). Measuring outflow rotation signatures using only the high-velocity jet counterparts is more challenging and requires more specialised observations (Coffey et al. 2004, 2007; Lee et al. 2017).

Outflows emission arises primarily from the cooling regions of the shocks generated when higher velocity material catches up with and impacts material ahead of it (Tsukamoto et al. 2023). While outflows are observed in all wavelength regimes, Class 0/I outflows are best observed with IR and sub-mm observations, as these wavelengths allow us to peer through the dusty envelope (Yang et al. 2022; Harsono et al. 2023; Beuther et al. 2023; Ray

et al. 2023; Nisini et al. 2024; Delabrosse et al. 2024). In particular, these outflows can be studied using IR Fe forbidden and H₂ ro-vibrational emission lines as these lines are brightly emitting near their bases and interestingly these two species trace different outflow components (Davis et al. 2011). [Fe II] emission traces hot, dense, partially-ionised, and high-velocity gas ($T \sim 10,000$ K; $n_e \sim 10^5$ cm⁻³; $v \sim 100$ km s⁻¹ - 400 km s⁻¹) (Nisini et al. 2002; Davis et al. 2003), while H₂ traces a molecular hydrogen emission line (MHEL) region associated with lower excitation, shocked molecular gas, or UV fluoresced gas, at much lower velocities ($T \sim 2,000$ K; $n_e \sim 10^3$ cm⁻³; $v \sim 10$ km s⁻¹ - 50 km s⁻¹) (Davis 2002; Caratti o Garatti et al. 2006; Frank et al. 2014). Therefore [Fe II] emission is a well established atomic jet tracer (Davis et al. 2003) and shocked H₂ emission is an important means of tracing molecular winds and cavities (Nisini et al. 2024). CO rotational emission lines at sub-mm wavelengths are also found in outflows from Class 0/I YSOs. The component of the outflow that CO likely maps is the resulting ambient gas after it has been swept up and entrained by some wide-angled wind and later left to cool (Arce et al. 2013), however in some cases it is thought to trace the disk wind itself (Louvét et al. 2018; de Valon et al. 2022). The CO emission traces molecular gas at low velocities also and is cooler than the H₂ emission ($T \sim 100$ K; $n_e \sim 10^3$ cm⁻³). Therefore, CO emission complements snapshots of current shock interactions obtained with H₂ and [Fe II] observations by providing us with an insight into the outflow history of the protostar (Richer et al. 2000).

Here SINFONI IFS observations of the HH 46/47 outflow system in the K-band (1.95 - 2.45 μm) are presented with a resolving power of $R = 4000$ (Fig. 1). HH 46/47 is an excellent prototype system for isolated star formation, located in the Bok Globule ESO 210-6A in the Gum nebula. See Sect. 2.1 for more details on the target. The field of view (FOV) chosen was 8''0 × 8''0 resulting in an observation of the base of the blue-shifted outflow. These observations allow us to investigate both the base of the fast axial jet and the wide-angled outflow component in near-infrared (NIR) [Fe II] and H₂ emission, and then comparison can be made with previous CO sub-millimeter observations. In particular, we wished to use a wavelength recalibration technique based on OH lines to search for a rotation signature in the HH 46/47 outflow. The target, observations, data reduction and data calibration are discussed in Sect. 2. In Sect. 3 we present the results of our observations, namely the morphologies and kinematics of the continuum emission, the wide-angled H₂ outflow cavity, and the base of the atomic jet. We also present a velocity gradient transverse to the outflow axis observed in the H₂ outflow cavity. In Sect. 4 we discuss our results. Included in our discussion is the observed layering of different emission tracers and the the origin of the velocity gradient associated with the H₂ outflow cavity. We summarise our conclusions in Sect. 5.

2. Target, observations, data reduction and calibration

2.1. HH 46/47

HH 46/47, discovered by Schwartz (1977), is a well studied complex of Herbig-Haro (HH) objects, series' of internal working surfaces or shock fronts in a larger outflow. The driving source of the outflow system (HH 46 IRS, HH 47 IRS, IRAS 08242-5050, 2MASS J08254384-5100326) is an embedded ($A_V > 35$), low-mass, Class I YSO binary system of $\sim 0''.26$ separation or 117 au (Reipurth et al. 2000; Nisini et al. 2024), taking a distance to the system of 450 pc (Graham & Heyer 1989). The source

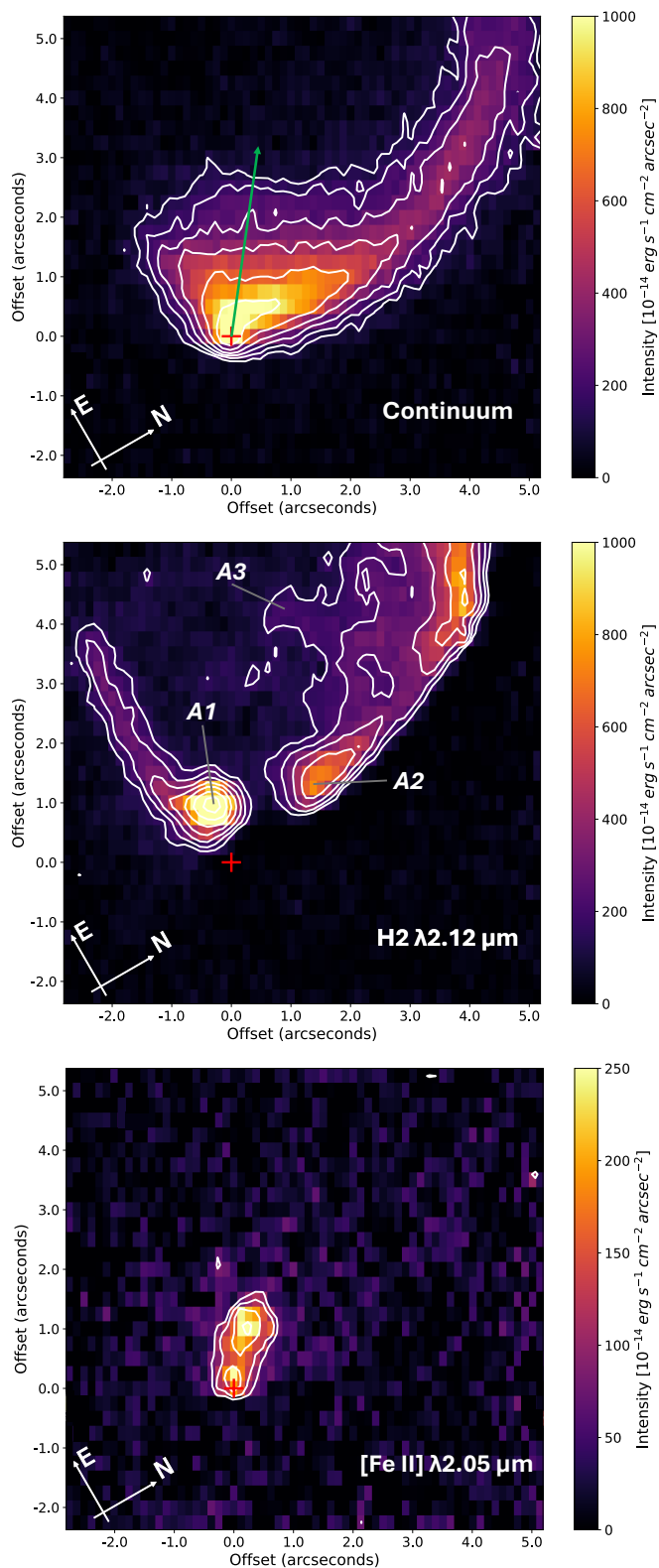


Fig. 1. Integrated intensity maps displaying the morphologies of the outflow in different emission tracers. The source position is marked with a red plus. Contour levels for all begin at 3σ of the background emission and increase by factors of 1.5. The vertical axis is aligned with centre axis of CO outflow (PA = 60°). *Top:* Continuum emission displaying a wide, approximately parabolic shape. Average jet PA of 52.3° indicated by a green arrow. *Centre:* Continuum subtracted and scattered light subtracted, integrated H_2 emission displaying a V-shaped outflow cavity. *Bottom:* Continuum subtracted, integrated [Fe II] emission displaying collimated atomic jet emission.

has a mass of approximately $1.2 M_\odot$ and bolometric luminosity of $< 15 L_\odot$ (Antoniucci et al. 2008), and is located at the north-eastern edge of the Bok globule, ESO 210-6A, in the Gum nebula. The bipolar outflow system consist of wide-angled, low-velocity, molecular outflows accompanied by highly-collimated, high-velocity, mainly atomic jets. The blueshifted side of the jet emanates north-easterly from the Bok Globule, making it easily visible at optical wavelengths (Heathcote et al. 1996; Hartigan et al. 2011). The redshifted side of the jet penetrates south-westerly, deep into the cloud, making it, and the driving source itself, visible at only infrared wavelengths (Eisloffel & Mundt 1994; Reipurth et al. 2000; Noriega-Crespo et al. 2004; Erkal et al. 2021b).

The blueshifted jet displays a screw-like structure that spirals counter-clockwise towards the observer with an angle of inclination of 37° with respect to the plane of the sky (Hartigan et al. 2005). Proper motions at the base of the jet are approximately 270 km s^{-1} and increases to 300 km s^{-1} (Hartigan et al. 2005; Erkal et al. 2021b). Wide-field images reveal that HH 46/47 extends at least 2.6 pc from the driving source, setting a lower limit to the dynamical age of the outflow of $10^4 - 10^5$ years old (Stanke et al. 1999). The jets display a prominent ‘wiggling’. It was postulated that the orbital motion of an unresolved tertiary component caused the meandering of the jet (Reipurth et al. 2000) as the separation of the binary system was too large to explain the short wiggling period of ~ 200 yr of the jet seen at large scales. The jet also displays a highly structured morphology, with knots seen along the outflow implying episodic ejection of material from the driving source.

The wide-angled molecular outflows have been well studied using ALMA CO (1-0) observations (Arce et al. 2013; Zhang et al. 2016) and CO (2-1) observations (Zhang et al. 2019). The low-velocity, wide-angled CO outflow is highly asymmetric, with the redshifted lobe extending four times further than blueshifted lobe, a lack of dense material in the path of the blueshifted flow is responsible for this. This wide-angled component displays multiple shell-like structures and these shells trace the ejection variability just like the collimated component of the outflow (Zhang et al. 2019). The variability timescales of the multiple outbursts seen in the wide-angle wind is consistent with episodic knots along the jet of HH 46/47. This suggests that the multiple shell structure seen in wide-angle component may arise from the same high accretion rate episodes that is reflected in the knots in the jets.

H_2 emission was first detected in the HH 46/47 system by Schwartz (1983) with the identification of six fluorescent UV emission lines produced by Ly- α pumping of H_2 . These molecules had to be first warmed to the second vibrational state of the electronic ground state. Later, NIR H_2 quadrupole emission in HH 46/47 was detected by Wilking et al. (1990). Eisloffel & Mundt (1994) first presented the H_2 morphology of the HH 46/47 system using the IRAC2 instrument on the ESO/MPI 2.2 m telescope. Noriega-Crespo et al. (2004) imaged the system in the near to mid-infrared using the Spitzer Space Telescope revealing the optically invisible redshifted jet propagating southwesterly revealing a loop-like morphology, with both outflow lobes being narrower than those observed in CO emission. Garcia Lopez et al. (2010) used long-slit NIR spectroscopic observations of the system using ISAAC and investigated the kinematics of the atomic and molecular emission, namely H_2 and [Fe II] emission, along the jet.

Erkal et al. (2021b) mapped the HH 46/47 system with HST with, at the time, unprecedented detail and recently, the HH 46/47 driving source and outflow were mapped at higher angu-

lar resolution of $\sim 0''.2$ with JWST using the NIRSpec IFU and MIRI MRS as part of the PROJECT-J program (ID 1706, P: B. Nisini) (Nisini et al. 2024). These observations provide unprecedented detail of the structure of the jet, the associated molecular outflow, and the cavity. Emission in H_2 reveals a complex molecular outflow, where the bright outflow cavity, expanding molecular shells and jet-driven bow-shocks interact with, and are influenced by ambient conditions. The superior spectral resolution provided by our SINFONI observations with respect to JWST ($R = 4000$ vs 2700), allows the outflow kinematics to be studied with unprecedented detail.

2.2. VLT SINFONI

Observations of the HH 46/47 outflow were obtained with the Spectrograph for INtegral Field Observations in the Near Infrared (SINFONI) on the 27th of November 2018 under ESO Program ID 0102.C-0615(A) (PI: C. Dougados). The NIR observations were obtained using the K-band grating ($1.95 - 2.45 \mu\text{m}$) with a resolving power of $R = 4000$. The FOV chosen was $8''.0 \times 8''.0$ providing a spatial sampling of $0''.125 \times 0''.250$ (Eisenhauer et al. 2003). This FOV was chosen as it was well suited to encompass the base of the outflow. The detector was rotated 60° so that the vertical axis of the detector was parallel to the approximate CO outflow position angle (PA) (Zhang et al. 2019). The observations consisted of ten exposures of 150 s each providing an on target exposure time of 1500 s. The average seeing of the science observation was $0''.81$. It was not possible to use the instruments AO correction due to a lack of a suitable bright point source nearby. Three exposures of 300 s were also taken for sky exposures. Two standard stars, HD 67954 (HIP 039774) and HD 73105 (HIP 042038), were also observed for flux calibration and telluric correction. The goal of the observations was to extract the 2-Dimensional (2D) spatial and kinematic distribution of atomic and H_2 emission lines at the base of the blueshifted outflow cavity.

2.3. Data reduction

The data was reduced using ESO's SINFONI data reduction pipeline (Version 3.3.0) and run with ESOReflex (Freudling et al. 2013). Standard calibration files were used. The datacube was corrected for bad pixels, flat-fielding, bias and dark signal, sky emission and a first order wavelength calibration was done using arc lamp wavelength solutions. All emission line velocities discussed throughout are corrected for the Barycentric Earth Radial Velocity (BERV) and the Local Standard of Rest (LSR) velocity of the cloud that the outflow emanates from, which is $+5.3 \text{ km s}^{-1}$ (van Kempen et al. 2009). The kinematical measurements presented here are therefore expressed with respect to the frame of the central source.

2.4. Wavelength recalibration

The spectral resolution of SINFONI in the K-band is approximately $R = 4000$ or 2.45 \AA , which translates to a velocity resolution of 75 km s^{-1} . The spectral sampling size in terms of velocity is 38 km s^{-1} at $1.95 \mu\text{m}$ and 30 km s^{-1} at $2.45 \mu\text{m}$. The wavelength calibration was performed using the standard procedure with the SINFONI data reduction pipeline. Wavelength calibration errors of approximately $\pm 30 \text{ km s}^{-1}$ were observed, by fitting OH telluric emission lines from Earth's upper atmosphere, in the final datacube after data reduction using the SIN-

FONI pipeline, which are not optimal for kinematical analysis. In order to increase the velocity calibration accuracy, a more rigorous wavelength calibration technique was employed. The data was run through the data reduction pipeline again, but the sky subtraction step was omitted from the process. This resulted in a datacube that contained the OH telluric emission lines. As these lines have a radial velocity of 0 km s^{-1} with respect to Earth's surface, they serve as a valuable tool for wavelength calibration. A 2D wavelength correction map could be produced using these OH lines as a velocity reference point, accounting for possible wavelength drifts across the FOV of the observation.

A cross-correlation method was employed to produce this 2D wavelength correction array by comparing the OH emission lines present in the science cube spectra with a theoretical night-sky spectrum. The cross-correlation routine used was from the Toolkit for Exoplanet detection and characterization with IfS (TEXTRIS) (Bonney et al. 2014; Petrus et al. 2021; Palma-Bifani et al. 2023; Demars et al. 2023). The ESO SKYCALC tool (Noll et al. 2012; Jones et al. 2013) was used to generate a synthetic night-sky spectrum that matched the night of observation and observatory location. The synthetic spectrum had a spectral resolution of $R = 100,000$ and was convolved with a Gaussian in order to downscale the spectral resolution to match that of the SINFONI K-band observations.

The cross-correlation procedure compares the spectral positions of the OH lines in the science cube with the theoretical positions in the synthetic night sky spectrum, and calculates the wavelength offset between the two around a desired spectral region. The cross-correlation method was run in a spectral region centred on the H_2 $2.12 \mu\text{m}$ emission line with care taken to avoid large telluric absorption bands within the spectral window. A 2D wavelength correction map was produced, where each pixel in the map corresponded to a wavelength offset between the OH lines in the science spectra and theoretical spectrum. A linear trend was observed in each of the horizontal rows of pixels in the 2D map. This trend is in accordance with the orientation of the horizontal slicing mirrors of the beam splitter present in the SINFONI Integral Field Unit (IFU). Each horizontal row of pixels in the 2D wavelength correction map was isolated and a linear fit was applied to the data points. Each linear fit was compiled into a 2D wavelength correction map. This wavelength correction map is shown in the appendix in the central panel of Fig. A.1. This method of precise wavelength calibration was also performed on SINFONI observations in Delabrosse et al. (2024).

This final wavelength correction map was applied to the SINFONI datacube, effectively obtaining a more accurate wavelength calibration than that offered with the standard arc lamp wavelength calibration. The relative uncertainty associated with this wavelength correction map, calculated from the standard deviations of the residuals of the horizontal linear fits, is $\pm 0.55 \text{ km s}^{-1}$. The absolute error associated with the map is estimated to be $\pm 0.62 \text{ km s}^{-1}$, calculated by computing the wavelength correction map in several narrow wavelength intervals throughout the spectral axis, allowing us to estimate the variation in wavelength (velocity) correction values as a function of the central wavelength. Summing the absolute and relative error in quadrature we retrieve the total uncertainty of the wavelength calibration procedure to be $\pm 0.83 \text{ km s}^{-1}$. Note that this value is not the final uncertainty on individual line centroid velocities.

There are also systematic errors that arise when using this wavelength calibration method that must be considered, as a single average wavelength correction value is derived for each spaxel over a wavelength range. Delabrosse et al. (2024) noticed

when applying the 2D wavelength correction map to single OH lines in the vicinity of the H₂ 2.12 μm emission line, there existed systematic offsets from the OH line's actual wavelength. These systematic uncertainties produce absolute errors of the order of 0.4 km s⁻¹, retrieved from Gaussian centroid offsets from the OH lines' known wavelengths, and relative uncertainties of the order of 0.9 km s⁻¹, retrieved from the standard deviation of wavelength correction values in the 2D wavelength correction map applied to the OH lines. We adopt the same values as we find similar results, as expected using the same wavelength calibration method. We therefore estimate a 1 σ uncertainty associated with the wavelength calibration of ± 1.0 km s⁻¹.

2.5. Uneven slit effect correction

The uneven slit effect is an instrumental limitation associated with spectrometers due to the non-uniform illumination of the slit, or an illumination gradient within the slit. In the case of IFUs, the slicing mirrors, which individually behave like long-slit spectrographs, are illuminated non-uniformly, introducing a spurious wavelength shift in the spectral axis between on-axis and off-axis light. Incoming light that enters the slicing mirror or slitlet at a point above the slitlet centre will have an opposite wavelength bias when compared with incoming light entering the slit at a point below the slitlet centre (Whelan & Garcia 2008). In the case of these observations, the effect arises due to the slope of the PSF creating a non-uniform brightness gradient within the slit. The resulting spurious wavelength shift depends on how strong the local brightness gradient is across the slit.

The generation of a further 2D wavelength correction map was necessary in order to correct for these illusory wavelength shifts due to uneven slit illumination. In our case, we endeavoured to generate a wavelength correction map for the H₂ 2.12 μm emission line as we required optimal confidence in the radial velocity measurements of the molecular outflow. In the case of SINFONI, the horizontal slicing mirrors can introduce spurious wavelength shifts up to a few km s⁻¹ (Agra-Amboage et al. 2014). The wavelength correction map due to uneven slit illumination was generated following the formulation developed by Marconi et al. (2003). This method is used successfully in Erkal et al. (2021a) and Agra-Amboage et al. (2014). The correction for the uneven slit effect is explained further in Sect. B of the appendix. Figure B.1 displays the resulting 2D wavelength correction map to amend for uneven slit illumination, generated for the H₂ 2.12 μm emission line, was applied to the datacube around this emission line of interest.

2.6. Flux calibration and telluric correction

Flux calibration was performed on the SINFONI datacube using the two standard star observations that were part of the same observation run. The standard star observations, HD 67954 (HIP 39774) & HD 73105 (HIP 42038), were reduced with the SINFONI data reduction pipeline in the same fashion as the science cube. Apertures, slightly larger in size than the seeing disc radius, were placed over the standard star's stellar positions and integrated to obtain the total flux with a high S/N. Annuli were used to estimate the contribution from the local background, which was subsequently subtracted from the aperture integration. Integrated stellar spectra were extracted using this method. The standard star's known magnitudes in J, H and K were obtained from the 2MASS catalogue (Skrutskie et al. 2006) and these magnitudes were converted to flux densities. Using the

Rayleigh-Jeans approximation of Planck's radiation law a flux vs. wavelength plot could be produced in order to calibrate the stellar spectra. The average calibration curve obtained independently from both of the standard star observations was used to flux calibrate the science data cube. The telluric contamination present in the observation was also corrected using the standard star observations. Each spectrum present in the science observation was divided by a normalised telluric correction spectrum obtained from the standard star HD 73105.

2.7. Continuum subtraction and scattered emission removal

The top panel of Fig. 1 in Sect. 2.1 displays a continuum image, integrated over $\lambda 2.190 \mu\text{m} - \lambda 2.191 \mu\text{m}$, which represents the same number of datacube slices as the integrated H₂ and [Fe II] images displayed in the central and bottom panels. The continuum emission is tracing a reflection nebula with an approximate parabolic shape that is asymmetric in intensity about the average jet PA of 52.3° from Erkal et al. (2021b) indicated by a green arrow in the top panel of Fig. 1. This reflection nebula is light from the driving source of the outflow scattered off the walls of the cavity, revealing the extent of the scattered light component present in these images, this contribution is present at all wavelengths.

As we endeavoured to investigate spectro-images of the outflow in intrinsic line emission, the scattered emission first needed to be removed. As the cavity was fully illuminated in continuum emission, an assumption was made that the scattered light component was entirely light from the unresolved central binary reflecting off the cavity. A spectrum was extracted from the continuum peak position (or the source position) to best represent the scattered emission contribution. A polynomial fit was applied to this source spectrum in order to rescale the source spectrum to the same level as the continuum at each spatial-pixel (spaxel) in the datacube. Subsequently, the rescaled source spectrum was subtracted locally in wavelength around each emission line of interest from the spectra at each spaxel. This effectively removed the scattered light component and continuum emission from the emission line of interest, leaving only the intrinsic line emission. This scattered emission removal routine was performed locally in the spectral region around each emission line of interest to ensure an accurate subtraction of scattered light. See Fig. C.1 in the appendix for a before and after of the scattered emission removal routine applied to H₂ emission.

Line to continuum ratio plots are an effective tool for investigating the contribution of scattered emission and for checking the effectiveness of any process for removing it. These plots display the result of calculating the ratio between an integrated line image and an integrated continuum image, taken spectrally nearby to the line of interest. The contribution from scattered light to the integrated line images will be represented by a constant ratio in these plots, as the scattered light follows the same spatial distribution as the continuum emission. In contrast, the real, intrinsic local emission will appear bright in these images, exceeding the constant ratio that represents the contribution from scattered light. The top left panel of Fig. 2 displays the result for H₂ emission. It is seen that the intrinsic line emission here is coming from the cavity walls and the H₂ knots at the bases of the cavity walls, in agreement with the central panel of Fig. 1. Intrinsic emission appears brighter as offset from the source increases as the contribution from scattered light decreases with distance from the source. This is why the tips of the northern and eastern cavity walls have significantly larger ratio values.

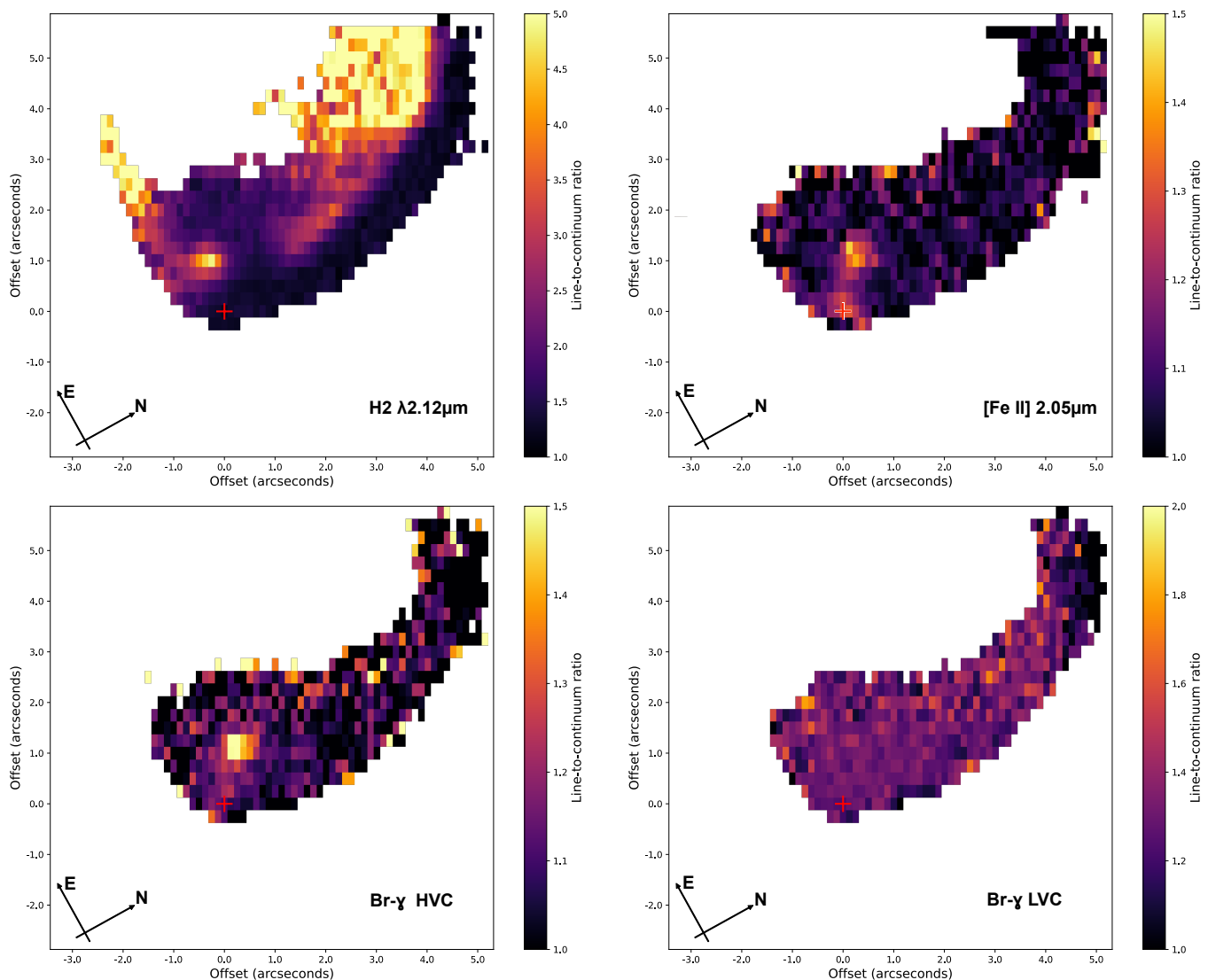


Fig. 2. Line-to-continuum ratio plots of H_2 , $[\text{Fe II}]$, and $\text{Br-}\gamma$ emission. Intrinsic emission appears bright in these images, whereas scattered light is represented by a constant ratio close to unity. The source position is represented with a red plus symbol. A signal-to-noise threshold, set at 3 times the background noise, is implemented in these images to reject background emission, meaning the morphologies we see in these figures is due to a combination of the continuum and the intrinsic line emission. *Top left:* Integrated H_2 emission between -140 km s^{-1} and $+60 \text{ km s}^{-1}$, divided by nearby continuum. Intrinsic line emission here is coming from the cavity walls and a H_2 knot at the base of the left cavity wall (A1). *Top right:* Integrated $[\text{Fe II}]$ emission between -310 km s^{-1} and -100 km s^{-1} , divided by nearby continuum. Intrinsic line emission we see here traces the high velocity atomic jet. *Bottom left:* Integrated high-velocity $\text{Br-}\gamma$ emission between -230 km s^{-1} and -130 km s^{-1} , divided by nearby continuum. Intrinsic line emission we see here, again, traces the high velocity atomic jet. *Bottom right:* Integrated low-velocity $\text{Br-}\gamma$ emission between -100 km s^{-1} and $+100 \text{ km s}^{-1}$, divided by nearby continuum. There is no spatially extended intrinsic emission detected here.

As the scattered emission subtraction process samples the representative scattered emission spectrum from the continuum peak, the base of the jet, traced in forbidden iron emission and $\text{Br-}\gamma$ emission, is removed as an unavoidable byproduct of the process, as jet emission is more compact and closer to the source position. This implies that some intrinsic atomic jet emission is present in the representative scattered emission spectrum or source spectrum due to the diameter of the aperture used to sample the spectrum, and also the angular resolution of the observation. As we were sacrificing the ability to trace the jet back to the source when applying this process to the jet tracing emission lines, we chose to not perform the scattered emission removal process from the jet tracing lines.¹

¹ This is also true for the H_2 emission originating on or near the source position. However, we recover very little to no intrinsic H_2 emission on

The top right panel of Fig. 2 presents the line to continuum plot for the $[\text{Fe II}]$ emission. There is little contribution from the scattered emission to the integrated line emission image of the jet, seen in Fig. 1 as the morphologies are similar, supporting our decision to not perform scattered emission subtraction on this emission line. The high-velocity (-230 km s^{-1} to -130 km s^{-1}) $\text{Br-}\gamma$ emission line to continuum plot is displayed in the bottom left panel of Fig. 2, and is seen to trace the jet also. Therefore scattered emission subtraction was not performed on this emission line either. A baseline continuum subtraction routine was

or near source in our data and so we could proceed with the scattered emission removal routine for molecular hydrogen. The low emission on or near the source position is confirmed by the line to continuum plot shown in Fig. 2. Regions immediately in the vicinity of the source position here display little to no intrinsic H_2 emission.

instead implemented by performing local polynomial fitting to the continuum around the emission lines. This polynomial fit continuum subtraction was performed at every spaxel in the datacube, for each emission line, with care taken to exclude the line emission region from the baseline fit.

In the bottom right panel of Fig. 2, we present a line to continuum map of low velocity Br- γ emission, integrated from -100 km s^{-1} to $+100 \text{ km s}^{-1}$. In this line to continuum map, the ratio of integrated line emission to continuum is approximately constant across the morphology of the cavity, and equal to the ratio located at the continuum peak position. We can infer from this that any spatially extended Br- γ emission we see in the low velocity interval follows the same spatial distribution as the scattered light seen in continuum. This implies that any extended, low velocity Br- γ emission is not intrinsic emission and is instead dominated by scattering of the central source spectrum off of the dusty, nebulous cavity material traced by the continuum.

3. Results

The SINFONI observation of HH 46/47 reveals emission lines tracing outflow and accretion activity, in agreement with previous spectroscopic studies (Antoniucci et al. 2008; Garcia Lopez et al. 2010). In this paper we discuss the morphology and kinematics of the jet and wide-angled outflow with a particular focus on the kinematics. Figure 1 presents integrated intensity maps which showcase the morphology of the HH 46/47 blue-shifted outflow. Maps of the continuum emission, molecular hydrogen (H_2) emission at $2.12 \mu\text{m}$, and forbidden iron emission at $[\text{Fe II}] \lambda 2.047 \mu\text{m}$ are shown. The H_2 emission line at $2.12 \mu\text{m}$, hereafter referred to as H_2 , is the brightest MHEL in the dataset that does not suffer any negative effects due to closeness to the spectral edge of the detector. The forbidden iron emission line at $2.047 \mu\text{m}$, hereafter referred to as $[\text{Fe II}]$, is the brightest iron emission line in the dataset. The source is partially embedded at these wavelengths but we detect a point source at the apex of the cavity in continuum emission. We fit a 2D Gaussian profile to this continuum peak and use this as our driving source position throughout. This continuum peak is not necessarily coincident with the position of the HH 46 IRS millimeter position derived by Arce et al. (2013) as in the IR, it is possible that the significant contribution of scattered light could shift the barycentre of the source continuum peak. A spectrum extracted from the source position is presented in Fig. 3. Atomic jet emission is identified in the FELs of $[\text{Fe II}]$, and in Br- γ emission. Several H_2 ro-vibrational emission lines ($v = 1-0$ & $2-1$) are detected, likely due to a wide-angled outflow cavity (see Sect. 3.1). In addition, CO overtone bandhead emission at $2.29 - 2.36 \mu\text{m}$, which traces the inner gaseous disk is also seen²

3.1. Morphology

The top panel of Fig. 1 as discussed in Sect. 2.7 displays a continuum image, integrated over $\lambda 2.190 \mu\text{m} - \lambda 2.191 \mu\text{m}$, which represents the same number of datacube slices as the integrated H_2 and $[\text{Fe II}]$ images displayed in the central and bottom panels. The morphology of the reflection nebula is approximately parabolic, and asymmetric in intensity about the average jet PA of 52.3° from Erkal et al. (2021b), indicated by a green ar-

row. The scattered light in the continuum image delineates the boundary region between the outflow and the ambient material, sweeping out a wide-angled hollow cavity in the quiescent material. The boundary region we see is essentially the cavity walls. The structure of the cavity as traced by continuum emission, CO emission and H_2 emission is discussed further in Sect. 4.2. The northern arm of the cavity extends further from the source than the eastern arm, suggesting a dissymmetry in the distribution of ambient material surrounding the outflow. The position of the driving source of the outflow is marked with a red plus symbol.

The central panel displays the continuum subtracted and scattered emission subtracted H_2 1-0 S(1) emission, integrated over radial velocities of $v = -95 \text{ km s}^{-1}$ to $+110 \text{ km s}^{-1}$. As also shown by the JWST NIRSpec H_2 $2.12 \mu\text{m}$ image in Nisini et al. (2024), the integrated H_2 emission has a striking V-shaped morphology tracing the limb-brightened cavity walls of the outflow. The shocked northern cavity wall traced by H_2 emission lies within the cavity structure seen in the continuum image, meaning the H_2 emission is confined within the outflow cavity seen in scattered light. This narrowing of the cavity walls suggests that the H_2 emission is probing deeper into the outflow cavity, allowing us to see within the cavity walls traced in scattered light. The H_2 cavity is again asymmetric about the jet PA with the northern wall appearing significantly brighter and extending further than the eastern wall. There is also some faint emission present within the cavity, especially apparent close to the interior of northern cavity wall. This emission within the cavity walls signifies that the cavity structure we see has a 3-Dimensional inverted-conical shape extending from the source and surrounding the atomic jet. The jet is not detected in H_2 . A bright H_2 knot of emission is also seen at the base of the eastern cavity wall at a distance of approximately $1''.0$ (450 au) from the source position. We label this bright H_2 peak *A1* following Nisini et al. (2024). We also label the dimmer H_2 peak at the base of the northern cavity wall at approximately $1''.4$ from the source position *A2*, and the arc-like structure extending from the northern cavity wall, curling towards the jet axis *A3*, again, following Nisini et al. (2024).

The bottom panel of Fig. 1 is the continuum subtracted, but not scattered emission subtracted, $[\text{Fe II}]$ emission at $2.047 \mu\text{m}$, integrated over radial velocities of $v = -280 \text{ km s}^{-1}$ to -65 km s^{-1} . $[\text{Fe II}]$ forbidden emission lines are well established atomic jet tracers. The $[\text{Fe II}]$ emission traces the base of the high-velocity, collimated jet, culminating in a bright knot or bow shock approximately $1''.0$ (450 au) from the source position. The jet bends slightly, tending towards the northern cavity wall as the jet PA (52.3°) and CO outflow PA (60°) are different from one another. An interesting observation is that the jet knot we trace with $[\text{Fe II}]$ does not coincide with the bright knot, *A1*, seen in H_2 emission, as seen in Nisini et al. (2024). There is a horizontal offset of approximately $0''.53$ (240 au) between the centres of these outflow emission knots. This offset between the jet knot seen in $[\text{Fe II}]$ and the outflow knot, *A1*, seen in H_2 suggests that the atomic jet emanates within the H_2 cavity, extending between the bases of the cavity walls seen in H_2 . Again, this indicates that the conical outflow cavity traced by molecular hydrogen surrounds the more collimated and faster moving atomic jet. The morphology of the high-velocity (-230 km s^{-1} to -130 km s^{-1}) Br- γ emission is almost identical to that traced by $[\text{Fe II}]$, displaying the base of the jet and the same knot at $1''.0$ from the source position. This is shown in the bottom left panel of Fig. 2. The Br- γ emission is discussed further in Sect. 3.2.

² Spectra extracted from an atomic jet knot at $1''.0$ (450 au) offset from the source position, and from both emission peaks (*A1* & *A2*) either side of the V-shaped cavity traced by molecular hydrogen (H_2) are also presented in Fig. D.1 of the appendix.

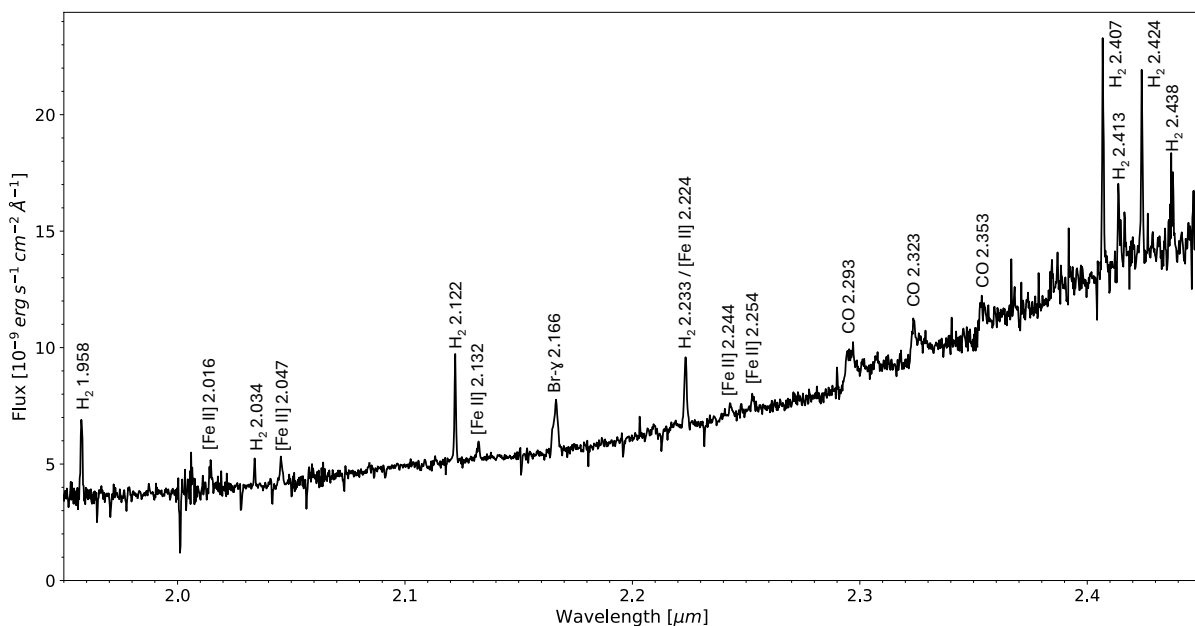


Fig. 3. Spectrum extracted using a circular aperture of radius $0''.41$ from the continuum peak. The jet emission is identified in the FELs of [Fe II], and in Br- γ emission. The outflow is detected in the H₂ emission lines. In addition, CO overtone bandhead emission at 2.29–2.36 μm , which traces the inner gaseous disk, is also seen. A characteristic reddening slope is evident in this spectrum as expected as the source is heavily extinguished and only visible at infrared wavelengths. Stellar absorption lines were not identified in this spectrum, it was concluded that the central source is too heavily extinguished to study these lines.

3.2. Kinematics

Position velocity (PV) diagrams can be extracted from integral-field spectroscopic data. A pseudo-slit is placed along the desired emission region, the spatial information within the slit is collapsed and represented by one axis and the wavelength information is converted into a radial velocity using Doppler shift and represented on the other axis. Figure 4 displays two PV diagrams, taken along the outflow axis, with a PA of 60° , from Zhang et al. (2019), and a pseudo-slit width of $1''$.

The top image in Fig. 4 displays a PV diagram extracted along the PA of the CO outflow axis in [Fe II] emission. Here we see emission traced from the source position at $0''$ culminating in a knot at $\sim 1''.0$ or 450 au. The radial velocity of the emission peaks at approximately -200 km s^{-1} , as is expected for a collimated atomic jet. A Gaussian profile was fit to the emission peak at offset $1''.0$, along the velocity axis, and a Gaussian centroid velocity of $v_{\text{LSR}} = -208.7 \pm 3.6 \text{ km s}^{-1}$ was retrieved. These radial velocities are consistent with previous observations (García Lopez et al. 2010; Nisini et al. 2024). In the bottom image of Fig. 4 a PV diagram, again taken along the PA of the CO outflow axis is shown, traced by Brackett- γ . The high velocity emission ($\sim -200 \text{ km s}^{-1}$) in this PV diagram is almost identical to that traced by [Fe II] implying that they are both tracing the jet. The high velocity emission again culminates in a knot at $\sim 1''.0$ or 450 au. Again, a Gaussian profile was fit to the emission peak at offset $1''.0$, along the velocity axis, and a Gaussian centroid velocity of $v_{\text{LSR}} = -211.9 \pm 3.5 \text{ km s}^{-1}$ was retrieved. A strong low velocity component at $\sim 0 \text{ km s}^{-1}$ with a full width extending to approximately $\pm 180 \text{ km s}^{-1}$ is also evident. As discussed in Sect. 2.7 the line to continuum map of this low velocity Br- γ emission, displayed in Fig. 2, implies that all of the extended, low velocity Br- γ emission is not intrinsic emission and is instead dominated by scattering. The intrinsic emission traced at approximately 0 km s^{-1} and having a full width extending to approximately $\pm 180 \text{ km s}^{-1}$, is very compact, spatially unresolved

emission entirely collocated at the source position, possibly tracing accretion processes and compact disk winds.

In Fig. 5 a PV diagram taken transverse to the outflow direction at a PA of 150° and at a distance of $1''.2$ above the source position is shown, traced by H₂ emission after scattered emission removal. This PA is perpendicular to the PA of the CO outflow axis. The width of the pseudo-slit used to extract this PV diagram is $0''.5$. The pseudo-slits position on the H₂ cavity is shown in the right panel of Fig. C.1, in the appendix. Notice that the radial velocity of material traced by H₂ is much lower than that traced by [Fe II] emission and Br- γ . Two emission peaks are seen either side of the source position, labelled A1 and A2. These emission peaks are the bases of each outflow cavity wall seen in H₂ emission in Fig. 1. We see that the emission peak from the eastern cavity wall (A1) peaks at a slightly higher radial velocity than the emission from the northern cavity wall (A2). A Gaussian fit was applied to both emission peaks in the velocity axis to retrieve the Gaussian centre of the emission. The Gaussian centroid velocity (v_{LSR}) of the emission peak A1 is $-33.9 \pm 1.4 \text{ km s}^{-1}$. The Gaussian centroid velocity of the emission peak A2 is $-16.9 \pm 1.5 \text{ km s}^{-1}$. These are highlighted on the figure. This difference in centroid velocity between the two sides of the cavity walls hints at the presence of a velocity gradient in the molecular cavity, transverse to the outflow direction.

3.3. H₂ velocity centroid map

The transverse PV diagram in H₂ emission hinting that both sides of the V-shaped outflow cavity had different radial velocities prompted the production of a 2D radial velocity map of the H₂ emission after scattered emission removal. The H₂ emission line at $2.122 \mu\text{m}$ is chosen here as it possesses the highest S/N of all of the H₂ emission lines in our observation and does not suffer any erroneous effects that are common near the spectral edges of IFU observations. The production of a 2D radial velocity map

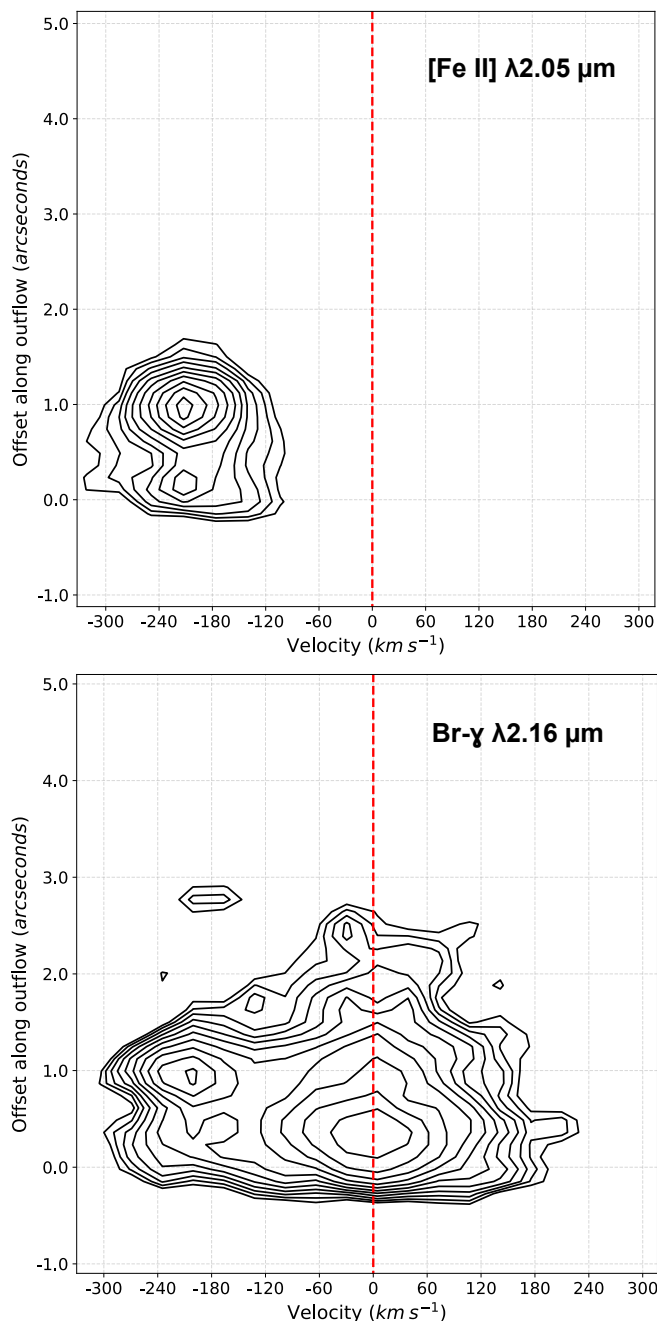


Fig. 4. *Upper:* PV diagram of the [Fe II] emission line region. The emission is traced from the source at $0''$ and culminates in a bow shock at $\sim 1''.0$ (450 au). The radial velocity of the jet emission traced in this line peaks at approximately -200 km s^{-1} , in agreement with previous observations. *Lower:* PV diagram of the Brackett- γ emission line region. The emission is again traced from the source and culminates in a bow shock at $\sim 1''.0$ (450 au). The radial velocity of the jet emission traced in this line peaks at approximately -200 km s^{-1} . The spatially extended low velocity Br- γ emission here, i.e. the emission centred around 0 km s^{-1} and having a full width extending to approximately $\pm 180 \text{ km s}^{-1}$, is not intrinsic emission, it is instead light scattered off of the nebulous cavity material. Contour levels for both begin at 3σ of the background emission and increase by factors of 1.2. Velocities are expressed with respect to the LSR.

of the H_2 emission was achieved by fitting Gaussian profiles to each H_2 emission line at every spaxel in the data cube and rejecting fits with a S/N below a certain threshold. The centres of

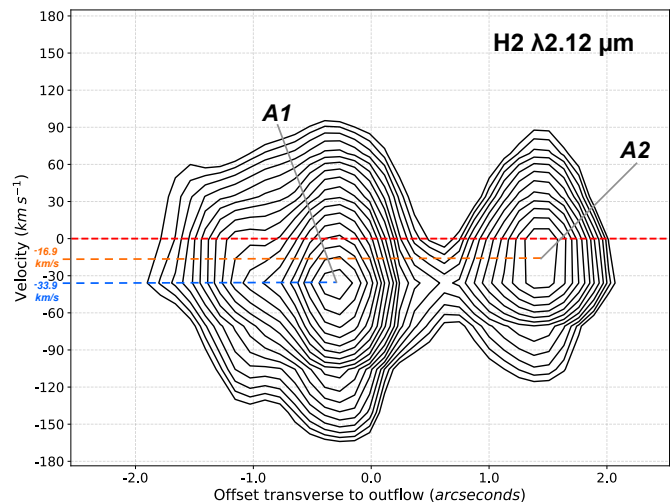


Fig. 5. Transverse PV diagram of the H_2 emission line region extracted at a projected z of $1''.2$ and with a pseudo slit width of $0''.5$. The radial velocity of the molecular emission is much lower than that of the atomic emission. Two emission peaks are seen either side of the source position, labelled A1 and A2. The emission peak on the left side of the cavity (A1) has a slightly higher radial velocity of -33.9 km s^{-1} than the emission peak on the right side of the cavity (A2) at -16.9 km s^{-1} . This hints at the presence of a velocity gradient transverse to the outflow direction in the cavity. Contour levels begin at 3σ of the background emission and increase by factors of 1.2.

each of the Gaussian profiles were taken as the centroid radial velocities of the emission line. This resulted in a 2-Dimension velocity centroid map of the H_2 $2.12 \mu\text{m}$ emission region shown in Fig. 6. The velocities in this map are expressed with respect to the LSR velocity of the cloud that the outflow emanates from. The error associated with the velocity centroid map is a combination of the uncertainty associated with the Gaussian fitting, namely the accuracy of the Gaussian centroid measurement and the uncertainty involved with the OH emission line wavelength recalibration. Thus, summing the relative and absolute errors in quadrature, we derive a 1σ uncertainty associated with the velocity centroid map of $\pm 1.0 \text{ km s}^{-1}$ to $\pm 3.0 \text{ km s}^{-1}$ depending on the brightness of the H_2 line.

We see the V-shaped cavity morphology reproduced in velocity centroid maps. The left image in the figure displays the integrated H_2 emission intensity map overplotted in black contour lines. The source position is marked with a black plus symbol. Here, -20 km s^{-1} was chosen as the centre point for the radial velocity gradient map. We see that the left outflow cavity wall has, on average, higher radial velocity peaks when compared to the right wall of the cavity. The velocity difference between both sides of the cavity is $\sim 10 \text{ km s}^{-1}$. In order to recover a more quantitative value for the radial velocity difference between both sides of the H_2 cavity, transverse PV cuts, similar to that presented in Fig 5, were taken at different heights (z) along the outflow. PV cuts of width $0''.25$ were taken at $z = 1''.0, 1''.5, 2''.0, 2''.5,$ and $3''.0$. The emission peaks corresponding to each side of the H_2 cavity in each PV plot were fit with Gaussian profiles along the velocity axis to retrieve the centroid velocity, in the same way the Gaussian centroid velocities were retrieved in Fig. 5. The difference in radial velocity centroid measurements (Δv_{rad}) between the left side of the H_2 cavity ($v_{\text{rad, left}}$) and the right side ($v_{\text{rad, right}}$), at each height (z) along the outflow, is presented in Table 1. The uncertainties associated with the centroid velocities are quadrature summations of the Gaussian centroid

Table 1. Velocity difference between eastern and northern pointing H₂ cavity walls at various heights along the outflow.

z (")	$v_{\text{rad, left}}$ (km s ⁻¹)	$v_{\text{rad, right}}$ (km s ⁻¹)	Δv_{rad} (km s ⁻¹)
1.0	31.3 ± 1.5	17.3 ± 2.5	14.0 ± 2.9
1.5	25.1 ± 2.0	13.4 ± 1.4	11.7 ± 2.4
2.0	24.0 ± 2.1	15.2 ± 1.4	8.8 ± 2.5
2.5	22.0 ± 2.3	16.6 ± 2.9	5.4 ± 3.7
3.0	22.8 ± 2.5	14.5 ± 2.0	8.3 ± 3.2

error and the uncertainty obtained with wavelength recalibration as discussed in Sect. 2.4.

The right image in Fig. 6 presents the same H₂ velocity centroid map, but integrated jet emission traced by [Fe II] in orange contours, and integrated Br- γ emission in green contours are overplotted instead. These emission lines are tracing the base of the jet. We see that the jet emission flows in-between either side of the H₂ cavity walls. This further illustrates that the H₂ low velocity gas is surrounding the high velocity jet in a conical morphology. This velocity gradient pattern observed between the eastern and northern pointing walls of the outflow cavity is also seen in the other molecular hydrogen emission lines present in our observation.

4. Discussion

Nisini et al. (2024) present spectacular JWST NIRSspec and MIRI observations of the HH 46/47 molecular outflow, cavity and atomic jet. Their NIRSspec 6" × 6" FOV encompasses a similar region to the SINFONI observations presented here but they have the advantage of the superior angular resolution of JWST. They suggest that A1 is an expanding bubble ejected by the secondary component of the binary system, as the A1 knot has a shell-like morphology revealed by the higher NIRSspec resolution and additional NIRCcam images. They associate both A2 and A3 with material entrained by the primary jet. The morphology of the H₂ emission obtained with SINFONI and seen in Fig. 1 further supports these conclusions. However, we cannot rule out with the SINFONI data alone that A1 and A2 instead trace the base of the cavity walls surrounding the jet. The spectral resolution of the Nisini et al. (2024) observations is $R \sim 2700$ which translates to ~ 110 km s⁻¹ of velocity resolution. The spectral resolution provided with SINFONI in the K-band ($R \sim 4000$) is superior, and the significant advantage of being able to perform a wavelength recalibration with OH lines (as described in Sect. 2.4) means that we can extract important kinematical information about the molecular emission and atomic jet which is not possible from the JWST observations.

4.1. Importance of removing scattered emission

The SINFONI observations presented here probe the launching region of an outflow, close to the embedded driving source. We were therefore conscious that our observations of various emission lines of interest would contain strong contributions of scattered light from the central engine. In order to study the emission lines of interest it was necessary to attempt to remove this contribution from scattered light and leave only intrinsic line emission. The contribution of scattered light to the intensity maps of various emission lines is clear in the line to continuum ratio plots in Fig. 2.

In this case, a simple baseline continuum subtraction method was sufficient in removing the continuum emission, however a

different method, as described in Sect. 2.7, was required to produce a clean observation free from scattered line photons emitted close to the central source. The line to continuum map of H₂ emission shown in the top left panel of Fig. 2 displays ratio values approximately between 1 and 2 in the inner region of the cavity and along the outer side of the northern pointing cavity wall. Here, the contribution from scattered light is strongest. Figure C.1 displays the integrated intensity map of the H₂ $\lambda 2.122$ μm emission line before and after the scattered emission removal routine was implemented. When comparing between these two images, it is clear that after the scattered light is subtracted there is a steeper intensity gradient associated with the intrinsic H₂ emission, which is most readily observable in the closeness of contour lines surrounding bright H₂ emission, such as the features labelled A1 & A2. Nebulous emission close the apex of the cavity has also been diminished after scattered light subtraction, which is in agreement with H₂ line to continuum map predicting a strong contribution from scattered photons in this region.

The work presented in this paper clearly highlights that for similar studies of outflows from embedded sources, it is critical to consider the contribution of scattered light to the emission line profiles and to acknowledge that removing the continuum emission using a baseline subtraction may not be optimal.

4.2. Layering of emission and axial asymmetries

The cavity seen in continuum emission surrounds the cavity traced by H₂ emission which in turn encompasses the collimated jet revealing a layered asymmetric outflow structure. To investigate this further we compared our SINFONI observations with HST and ALMA observations. Figure 7 displays the continuum subtracted [Fe II] $\lambda 1.64$ μm emission image of HH 46/47, obtained using HST WFC3 with the narrowband filter, F164N (Program ID: 15178, PI: B. Nisini) (Erkal et al. 2021b). The blueshifted jet extends north-easterly and the redshifted jet, south-westerly. The inset shows a 3-colour image made from the SINFONI observation of the outflow cavity and jet. Integrated continuum, or scattered light from the outflow driving source, is traced here in red. The continuum and scattered light subtracted, integrated H₂ emission is traced here in green. The SINFONI [Fe II] continuum subtracted emission, tracing the collimated atomic jet is displayed here in blue. Finally, the inner part of the HST [Fe II] $\lambda 1.64$ μm is overplotted in orange contours. For the inset, the HST contours have been rotated to match the 60° clockwise rotation that our SINFONI observations underwent. The HST image was aligned with the SINFONI image by coinciding the continuum peak positions, retrieved using 2D Gaussian fitting, located at the apex of the cavity in each image. Figure 8 displays an adapted figure from Zhang et al. (2019) of the blue and red-shifted molecular outflows from the HH 46/47 system in ¹²CO (2-1) as observed with ALMA. Here, blue traces integrated CO emission from -35 km s⁻¹ to -10 km s⁻¹, green traces the 1.3 mm dust continuum emission and, red traces integrated CO emission from +10 km s⁻¹ to +50 km s⁻¹. The blue-shifted cavity seen in H₂ emission is overplotted. The H₂ cavity has been rotated anticlockwise by 90° with respect to the SINFONI results presented earlier so that the outflow cavity axis points along the horizontal axis. The continuum peak position in the SINFONI image, marked with a red plus symbol, was aligned with the centre of the 1.3 mm dust continuum in the ALMA image. An inset displays a zoomed image of the H₂ emission overplotted on the blueshifted CO outflow to better illustrate that the H₂ emission is nested within the CO outflow. This inset has been rotated clockwise by 90° to match the convention of figures pre-

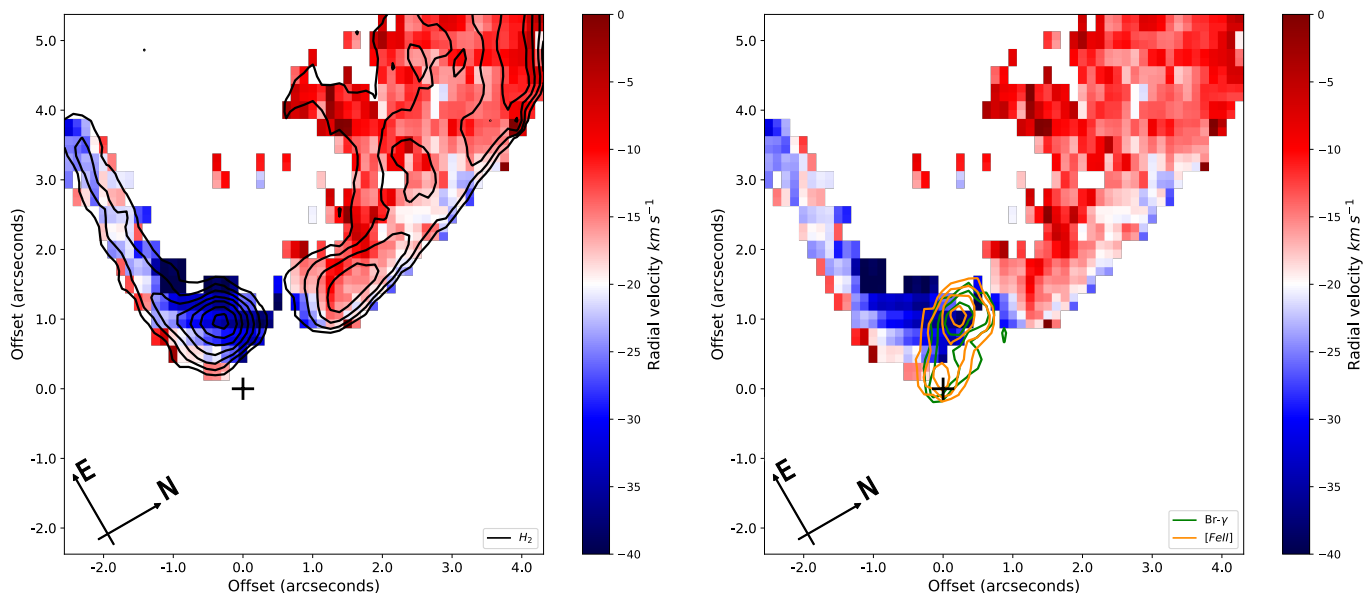


Fig. 6. Scattered light corrected H_2 emission radial velocity centroid maps. The source position is marked by a black plus symbol. The radial velocity centroid maps display a clear velocity gradient between both sides of V-shaped cavity. The left side of the cavity has, on average, a greater radial velocity when compared with the right side. The difference in velocity between both sides is $\sim 10 \text{ km s}^{-1}$. Contour levels for both begin at 3σ of the background emission and increase by factors of 1.5. *Left:* H_2 velocity centroid map with integrated H_2 emission overplotted in black contour lines. *Right:* The same H_2 velocity centroid map with jet-tracing integrated $[\text{Fe II}]$ emission in orange contours, and integrated $\text{Br-}\gamma$ emission in green contours overplotted. The jet flows between both sides of the cavity traced by H_2 .

sented in this paper, where the outflow axis is aligned with the vertical axis.

The comparison between SINFONI and HST shows that both sets of observations are consistent. The bending towards the northern cavity wall does not just occur for the $\sim 675 \text{ au}$ long SINFONI jet but continues out to $> 1000 \text{ au}$ in the HST jet. Also, the bright knot seen in $[\text{Fe II}] \lambda 2.047 \mu\text{m}$ emission in the SINFONI dataset coincides with a knot traced by the $[\text{Fe II}] \lambda 1.64 \mu\text{m}$ emission from the HST dataset. This is expected as the SINFONI observations took place in November 2018 and HST observations took place in March 2019, just four months later. As the jet knot radial velocity traced by $[\text{Fe II}] \lambda 2.047 \mu\text{m}$ emission is $\sim -200 \text{ km s}^{-1}$, the jet velocity in the plane of the sky is $\sim 265 \text{ km s}^{-1}$, or 56 au yr^{-1} , using a jet inclination value of 37° from Hartigan et al. (2005). We therefore expect the jet knot to have moved by just 14 au between observations. The pixel scale of the SINFONI observations is $\sim 56 \text{ au}$, meaning the expected offset would not be measurable. The $[\text{Fe II}] \lambda 1.64 \mu\text{m}$ emission displayed in orange contours appears to possess an additional knot coinciding with the H_2 knot A1 seen here in green, suggesting that the knot may also be traced in $[\text{Fe II}]$ emission. However, due to the low S/N, and the observation that this knot is not traced by any of the other $[\text{Fe II}]$ emission lines, we instead attribute this emission to residual unsubtracted continuum emission or scattered light.

The layered structure we see clearly in Figs. 7 and 8 is a radial stratification, not only morphological in nature but also in temperature, between hot gas ($T_{H_2} \sim 10^3 \text{ K}$) and the bulk of the surrounding colder material ($T_{CO} \sim 10^1 \text{ K}$). Not only do we see that the H_2 emission lies within the continuum emission, but we also see that the H_2 outflow cavity is nested within the blue-shifted $^{12}\text{CO} (2-1)$ cavity. The H_2 outflow cavity existing within the CO molecular outflow has been observed in HH 46/47 in Noriega-Crespo et al. (2004), with different emission lines than those presented here, and more recently in Nisini et al. (2024), showing that the mid-IR H_2 emission is nested within the CO

cavity in both the blue and red-shifted outflow lobes. At $\sim 4''$ along the outflow axis, the northern H_2 cavity wall begins to curl inwards towards the jet axis. This curling of the H_2 cavity is also seen in Nisini et al. (2024), that they interpret as material entrained by the expanding primary jet. Similarly, the eastern cavity wall lies within the CO molecular outflow and appears to possess a narrower opening angle. However, we note that CO opening angle close to the base is narrower than the CO cone farther away from the source, indicating that there is some sudden increase of the CO opening angle, especially evident in the east side at some distance. The inner, narrower CO cone has a morphology more consistent with the H_2 emission morphology. This comparison of the different emission tracers reveals a stratification between continuum emission, CO emission, H_2 emission, and the jet implying that outflowing material from the star/disk system is spatially layered as radial distance from the jet axis increases. The highest velocity, highest temperature, and most strongly collimated emission is located at the centre of the outflow axis and surrounding it is the slower moving, cooler, wide-angled molecular component of the outflow. This onion-like layered flow structure with stratification of emission in velocity, temperature, and chemistry has been observed in some cases (Delabrosse et al. 2024), and is predicted by MHD disk wind models (Ferreira 1997; Panoglou et al. 2012; Bai et al. 2016; Zhu & Stone 2018; Wang et al. 2019). In these models, material is accelerated along flow streamlines, poloidal magnetic field lines anchored in the rotating disk. Hot, high-velocity emission travel along streamlines originating in the very inner disk region, whilst cooler, lower velocity emission travel along streamlines originating further out in the disk. This stratified structure can be identified observationally when tracing the disk wind directly or tracing the winds interaction with surrounding ambient material. In this case, the CO is thought to be entrained material, tracing material located outside the cavity wall, whilst the H_2 emission is likely tracing the interaction region that put the entrained material into motion. The origin of such an interaction

can be explained by an MHD disk wind, but can also be produced by the jet alone. Consequently, we cannot conclusively attribute the onion-like stratified structure exclusively to an MHD disk wind.

The H₂ cavity is likely an interaction region between some wide-angled component of the outflow, be it an uncollimated or poorly collimated wind, or an expanding shell of material produced by a wide-angled wind, and the surrounding ambient material, or by the stacking of successive jet bowshocks from a collimated, variable inner jet propagating into a density-stratified surrounding medium (Rabenahary et al. 2022). It is possible that we are seeing nested cavities traced in H₂ similar to those seen in cooler CO emission caused by multiple expanding shells. These expanding shells of material have been observed in the blue-shifted and red-shifted outflows of HH 46/47, traced by ¹²CO emission (Zhang et al. 2019). These shells, which are highly coherent in space and velocity, have an parabolic morphology. The origin of these outflowing shells can be explained by entrainment of ambient material by an episodic wide-angle wind (Li & Shu 1996; Lee et al. 2000) which produces radially expanding parabolic shells, or by successive jet bowshocks. The general morphology of the H₂ cavity which lies within the cavity traced by continuum emission could be produced by expanding shells of material, interior to the shells identified in CO by Zhang et al. (2019). Furthermore, the emission peaks labelled A1 and A2 could potentially be tracing shocked interaction regions between a more evolved shell, traced by the outer cavity walls, and a smaller scale, asymmetric H₂ shell nested within, produced by a subsequent outburst of the wide-angled wind or a successive jet bowshock. The arc-shaped morphological component labelled A3 could also be associated with a cavity or shocked region created by an expanding shell.

It is clear that both the outflow cavity traced by H₂ emission and the atomic jet traced by [Fe II] and Br- γ emission are asymmetric about the CO outflow direction. The emission region of the left side of the cavity, that is, the eastern cavity wall, traced by H₂ is spatially more compact when compared to the right side, the northern cavity wall. The right side of the cavity also extends further from the driving source, both vertically and laterally. If the surrounding medium on the right side of the cavity side is denser than that of the left side, then this would naturally lead to brighter shocked wall regions on the right side of the cavity. The suggestion that the surrounding ambient material is denser on the right side of the cavity is further supported by the morphology of the scattered light emission seen in Fig. 1. Here, the cavity as seen in scattered light is highly asymmetric about the CO outflow axis with the northern arm extending much further from the driving source than the eastern arm. This further suggests a dissymmetry in the distribution of the surrounding ambient material. This inhomogeneous ambient material is further testified by the general morphology of the reflection nebula seen at optical wavelengths that extends mostly in the northern direction (Heathcote et al. 1996). Furthermore, in Fig. 8, the 1.3 mm dust continuum is clearly brighter on the northern side, supporting this argument. As mentioned before, there is some sudden increase of the CO opening angle, especially evident in the east side at between 2'' and 3'' additionally reinforcing this argument. The northern side of the outflow is facing the cloud edge that the blueshifted outflow is emanating from, which may be shaped or compressed by radiation from outside the cloud. This may provide a rationale for why the ambient material on the northern side appears denser. There also exists an offset between the average PA of the atomic jet, 52.3° from Erkal et al. (2021b), and the central axis of the wide-angled CO outflow, ~

60° from Zhang et al. (2019). This difference between the jet PA and molecular outflow PA can be interpreted as being due to an inhomogeneous surrounding medium, with the eastern cavity wall expanding quicker than the northern cavity wall and therefore shifting the central axis of the CO outflow to a larger PA than the jet PA.

We see that the atomic jet is deflected away from the left side of the cavity, tending towards the northern wall. Also, the jet knot traced by [Fe II] and Br- γ emission does not coincide with either peak traced at the bases of the cavity walls seen in H₂ labelled A1 and A2. The bending of the atomic jet towards the northern cavity wall is consistent with the [Fe II] λ 1.64 μ m emission from the HST observations. This bending of the atomic jet is indicative of jet wiggling, that is clearly seen in large scale observations of the jet (Reipurth et al. 2000; Erkal et al. 2021b). Jet wiggling can be induced by an orbiting companion to the outflow driving source (Murphy et al. 2021). These axial asymmetries seen in the blueshifted outflow, both in the atomic jet and the wide-angled outflow and cavity may also arise due to the influence of two outflows being driven by each of the components of the binary system (Nisini et al. 2024). The difference between the jet PA and molecular outflow PA can also be interpreted as being due to the secondary jet pushing on the eastern cavity wall, again shifting the central axis of the CO outflow to a different PA when compared to the jet PA.

4.3. Origin of the H₂ transverse velocity gradient

The V-shaped, parabolic cavity observed in the integrated H₂ emission in Fig. 6 displays a clear transverse velocity gradient of approximately ~ 10 km s⁻¹ between the eastern and northern pointing cavity walls, see Table 1. A transverse velocity difference, lower in magnitude, is also present in ¹²CO emission in the same sense as the velocity difference presented here (2024, priv. comm Y. Zhang). Whilst the spectral resolution of the SINFONI dataset is $R = 4000$ or 2.45 Å, which translates to a spectral sampling of 38 km s⁻¹ at 1.95 μ m and 30 km s⁻¹ at 2.45 μ m, we can be confident in a velocity difference of ~ 10 km s⁻¹ between either side of the cavity due to our wavelength recalibration performed using the OH lines from the upper atmosphere and discussed in Sect. 2.4. We obtained a 1σ uncertainty of ± 1.0 km s⁻¹ to ± 3.0 km s⁻¹ associated with this velocity centroid map, which encompasses absolute and relative errors associated with Gaussian centroid accuracy and the OH wavelength calibration.

Initially it may appear that this velocity gradient we see is due to the anticlockwise rotation of the H₂ cavity, with the eastern cavity wall approaching at a higher velocity with respect to the northern cavity wall. This apparent rotation may be tracing a rotating disk wind directly (Zhang et al. 2016), or tracing the rotation of entrained material, where the angular momentum present in the envelope is provided for by the jet (Gaudel et al. 2020). This rotation would support the MHD driven wind model as we expect a rotation of the outflow if the wind is removing angular momentum from the star/disk system. Rotating cavities have been observed in early to late stages of low mass star formation (Bjerkeli et al. 2016; Tabone et al. 2017; Zhang et al. 2018; Louvet et al. 2018; de Valon et al. 2022; Launhardt et al. 2023). In order to investigate the plausibility of this velocity gradient being caused by a rotation of the cavity, we assumed that the velocity gradient was purely due to rotational motion and calculated the specific angular momentum of this apparent rotation at different heights along the outflow. We derive the ve-

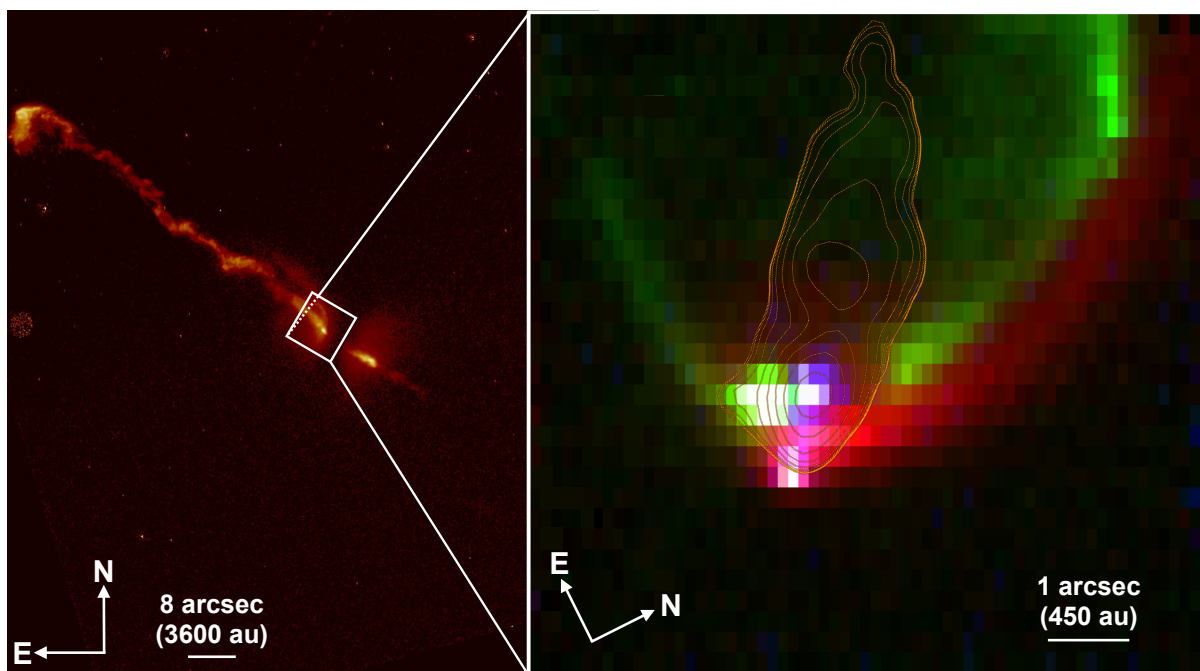


Fig. 7. *Background:* Continuum subtracted [Fe II] $\lambda 1.64 \mu\text{m}$ emission image of HH 46/47. Observation obtained using HST WFC3 with narrow-band filter F164N (Program ID: 15178, PI: B. Nisini) (Erkal et al. 2021b). *Inset:* SINFONI 3-colour image displaying the outflow cavity and jet. Red emission traces integrated continuum emission or scattered light from the outflow driving source. Green emission traces continuum subtracted integrated molecular hydrogen (H_2) emission displaying the V-shaped outflow cavity. The shocked cavity walls lie within the cavity structure seen in scattered light in continuum emission. There is a bright outflow knot at the base of the left cavity wall. Blue emission traces [Fe II] emission, displaying collimated atomic jet emission. The jet culminates in a bright knot or bow shock approximately $1''.0$ (450 au) from the source position. This knot does not spatially coincide with the outflow knot seen in H_2 emission. The inner part of the HST [Fe II] $\lambda 1.64 \mu\text{m}$ is overplotted in orange contours.

locity differentials from the H_2 velocity centroid map provided in Fig. 6, by extracting a transverse PV cut at a specific height along the outflow. Gaussian profiles are then fit along the velocity axis to both of the emission peaks corresponding to each side of the H_2 cavity, retrieving the centroid velocity of each side of the H_2 cavity, as described in Sect. 3.3. The rotational radius r is estimated, assuming the rotation is axisymmetric, as half of the distance between the two emission peaks corresponding to each side of the H_2 cavity. The uncertainties associated with the centroid velocities are quadrature summations of the Gaussian centroid error and the uncertainty obtained with wavelength recalibration as discussed in Sect. 2.4. The specific angular momentum ($J = r \times v_{\text{rot}}$) of a rotation or orbit is defined as the angular momentum associated with the rotation divided by the systems mass, in other words, the angular momentum per unit mass. Assuming that the flow is axisymmetric we can calculate the specific angular momentum as follows:

$$J(r) = r \times v_{\text{rot}}(r) = r \times \frac{v_{\text{left}} - v_{\text{right}}}{2 \sin(i)} \quad (1)$$

Where $v_{\text{rot}}(r)$ is the rotational velocity and i is the angle of inclination of the flow with respect to the line of sight, $i = 53^\circ$. Using Equation 1, we calculated the specific angular momentum of the apparent cavity rotation at heights along the outflow in the plane of the sky, of $z = 450 \text{ au}$, 675 au , and 900 au ($z = 1''.0$, $1''.5$, $2''.0$). The specific angular momentum results are presented in Table 2. We calculate specific angular momenta values of $J(r) = 3217 \text{ km s}^{-1} \text{ au}$, at $1''$ offset from the central source, to $3867 \pm 1125 \text{ km s}^{-1} \text{ au}$, at $2''$ offset.

In the case that the H_2 velocity gradient is directly tracing an outflow rotation we can compare to previous outflow rotation

observations. Bjerkeli et al. (2016) measure the specific angular momentum, in ^{12}CO emission, of the rotating outflow associated with the TMC1A protostellar system to be less than $200 \text{ km s}^{-1} \text{ au}$, using r values an order of magnitude lower than those used here. Zhang et al. (2018) measure the mean specific angular momentum, in C^{18}O emission, in the rotating NGC 1333 IRAS 4C outflow to be $100 \text{ km s}^{-1} \text{ au}$. Louvet et al. (2018) measure the specific angular momentum, in ^{12}CO emission, of the rotating HH 30 outflow to be $\sim 40 \text{ km s}^{-1} \text{ au}$. In de Valon et al. (2022), they measure the specific angular momentum, in ^{12}CO emission, of the rotating outflow from DG Tauri B to be $\sim 65 \text{ km s}^{-1} \text{ au}$. Launhardt et al. (2023) measure the specific angular momentum, in ^{12}CO emission, of the rotating outflow from a young T Tauri star in the CB 26 Bok globule to be less than $200 \text{ km s}^{-1} \text{ au}$. Zhang et al. (2016) estimated the specific angular momentum in the equatorial plane of the envelope surrounding HH 46/47 in ^{13}CO and C^{18}O emission. They found specific angular momentum values for the rotation of $J = 450 - 540 \text{ km s}^{-1} \text{ au}$ ($J = 2.2 \times 10^{-3}$ to $2.6 \times 10^{-3} \text{ km s}^{-1} \text{ pc}$), an order of magnitude lower than the specific angular momenta estimated here. As this rotation is measured in the equatorial plane, it is indicative of an upper limit for the specific angular momentum in this system. In the case that the H_2 velocity gradient is instead tracing the rotation of entrained material, where the angular momentum present in the envelope is provided for by the jet we can compare with Gaudel et al. (2020). They measure the specific angular momentum of the midplanes of circumstellar environments of a sample of class 0/I protostellar envelopes. In their sample, the maximum specific angular momenta values, at similar r values presented here, are $2 \times 10^{-3} \text{ km s}^{-1} \text{ pc}$ ($\sim 400 \text{ km s}^{-1} \text{ au}$), an order of magnitude below what we measure here.

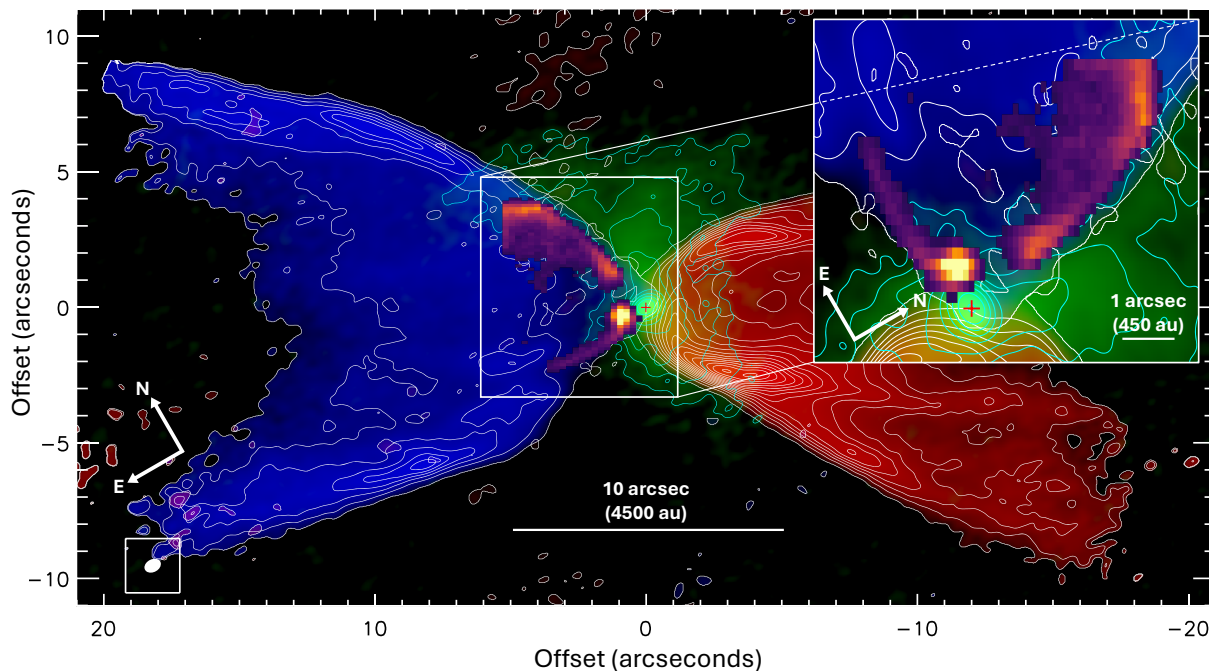


Fig. 8. SINFONI H₂ emission overplotted on the blueshifted molecular outflow traced by ¹²CO (2-1) as observed by ALMA (Zhang et al. 2019). Blue traces integrated CO emission from -35 km s^{-1} to -10 km s^{-1} . Green traces the 1.3 mm dust continuum. Red traces integrated CO emission from $+10 \text{ km s}^{-1}$ to $+50 \text{ km s}^{-1}$. The shocked cavity walls traced by H₂ lie within the cavity structure seen CO emission. The red plus indicates the continuum peak position in the SINFONI data. An inset displays a zoomed image of the H₂ emission overplotted on the blueshifted CO outflow to better illustrate that the H₂ emission is nested within the CO outflow. This inset has been rotated clockwise by 90° to match the convention of figures presented in this paper, where the outflow axis is aligned with the vertical axis. Figure adapted from Zhang et al. (2019).

Table 2. Specific angular momenta calculations of H₂ cavity rotation at various heights along the outflow.

z (au)	v_{left} (km s ⁻¹)	v_{right} (km s ⁻¹)	v_{rot} (km s ⁻¹)	r (au)	r (10 ⁻³ pc)	$J(r)$ (km s ⁻¹ au)	$J(r)$ (10 ⁻² km s ⁻¹ pc)
450	31.3 ± 1.5	17.3 ± 2.5	8.8 ± 1.8	365.6	1.8	3217 ± 658	1.6 ± 0.3
675	25.1 ± 2.0	13.4 ± 1.4	7.3 ± 1.5	506.3	2.5	3696 ± 759	1.8 ± 0.4
900	24.0 ± 2.1	15.2 ± 1.4	5.5 ± 1.6	703.1	3.4	3867 ± 1125	1.9 ± 0.6

The specific angular momenta calculated here at various heights along the outflow cavity are significantly larger than that seen before for rotating outflow cavities, either rotational motion traced directly by the outflow or by rotating entrained material. Furthermore, the apparent anticlockwise rotation we see here is opposite to the clockwise rotation of the flattened structure around the central source perpendicular to the outflow axis traced by ¹³CO and C¹⁸O from Zhang et al. (2016). Whilst this flattened structure has a size of approximately 10'' (4500 au) across, which is much larger than what is expected for a rotationally supported Keplerian disk, it is indicative of the disk rotation direction as the sense of rotation remains consistent as the beam size, in ¹³CO and C¹⁸O, is scaled down to its smallest size, 1''5 (675 au). They conclude that the structure is a rotating envelope that feeds the accretion disk. Although some jets present transverse velocity gradients in the opposite sense to the disk rotation (Cabrit et al. 2006; Louvet et al. 2016), it is unclear if these gradients (of a few km s⁻¹ and variable in time) truly trace counter-rotation of the jet, or if they are contaminated by other effects such as jet precession or shock asymmetries. The large specific angular momenta calculated here and the fact that the apparent rotation is opposite to the sense of the disk rotation lead us to rule out the interpretation that the velocity gradient observed in the H₂ cavity is entirely tracing a rotation signature and other effects must be considered.

Another possible explanation for the velocity gradient could be ascertained from the observation that the cavity seen in H₂ is clearly asymmetric about the outflow direction. If the surrounding medium in the region of the northern cavity wall is denser than that in the region around the eastern cavity wall, as discussed in 4.2, then the outflowing material, or expanding shells of material rather than a wide-angled wind, would encounter and impact denser quiescent material in the region of the northern cavity wall causing the outflow or shells to decelerate more quickly. This could explain why the northern wall of the cavity displays lower radial velocities when compared to that seen in the eastern wall. The denser quiescent material at the right side of the cavity could naturally explain the velocity gradient we see in the H₂ emission. The production of transverse velocity gradients due to dissymetry in density of surrounding ambient material has been discussed by De Colle et al. (2016).

Lastly, the velocity gradient seen in the cavity traced by H₂ emission could be that the dominating outflow driver for the northern and eastern cavity walls originate from different sources. The driving source of the HH 46/47 outflow system is known to be a binary source (Reipurth et al. 2000). Nisini et al. (2024) suggest that the bright H₂ knot seen at the base of the eastern cavity wall, A1, is an expanding bubble ejected by the secondary component of the binary system. This could imply that the emission we see in the eastern wall of the H₂ cavity could have been strongly influenced by this secondary outflow

driver. The outflow from this secondary source in the binary system could be strongly contributing to the shocked H_2 emission in the eastern wall of the cavity, potentially increasing its radial velocity in comparison to the northern wall. This is further testified by the H_2 knot *A1* possessing the highest blueshifted radial velocity in the velocity centroid maps provided in Fig. 6.

We would like to emphasise that velocity gradient signatures observed transverse to the outflow direction can easily be misinterpreted as being due to rotational motion, and this interpretation is further motivated by current MHD disk wind models. However, other effects, such as ambient material density variations and the presence of multiple outflows, as discussed above can produce transverse velocity gradient signals. In addition, further effects such as kink instabilities (Staff et al. 2014) and twin-jet structures (Soker et al. 2022), to name a few, can reproduce transverse velocity gradients. We investigated other interpretations of the observed velocity gradient due to our specific angular momentum values being significantly larger than that seen before for rotating outflow cavities, and due to the apparent counter-rotation of the outflow with respect to the conjectured disk rotation direction. However, other effects that can produce similar velocity gradient signatures must be considered in cases where specific angular momentum estimates are as expected and apparent rotation direction is in the same sense as the disk.

5. Summary and conclusions

We have investigated the morphology and kinematics of the launching region of the blueshifted HH 46/47 outflow, emanating from the Class I binary system HH 46 IRS, with SINFONI K-band observations. We achieve an angular resolution of $0''.81$ and a precision in velocity centroids (in H_2 1-0 S(1) emission) of ± 1 to 3 km s^{-1} . These observations allow us to study both the base of the atomic jet traced by $[\text{Fe II}]$ and $\text{Br-}\gamma$ emission and the wide-angled molecular hydrogen outflow. We summarise our main results as follows:

- We use PV diagrams, as seen in Sect. 3.2, to investigate the kinematics of the atomic jet and the H_2 outflow cavity. The radial velocity of the atomic jet emission traced by $[\text{Fe II}]$ and $\text{Br-}\gamma$ peaks at $\sim -210 \text{ km s}^{-1}$, which is consistent with previous measurements. The Gaussian centroid velocity of the atomic jet knot at an offset of $1''$ from the source position is $v_{\text{LSR}} = -208.7 \pm 3.6 \text{ km s}^{-1}$ in $[\text{Fe II}]$ emission and $v_{\text{LSR}} = -211.9 \pm 3.5 \text{ km s}^{-1}$ in $\text{Br-}\gamma$ emission. A PV diagram taken transverse to the outflow axis was taken to investigate the kinematics of the H_2 emission. The radial velocity of the H_2 emission is significantly lower than that of the atomic jet emission, peaking around $\sim -15 \text{ km s}^{-1}$ to -30 km s^{-1} . Two emission peaks located at the base of each cavity wall are seen either side of the source position, labelled *A1* and *A2*. The emission peak from the base of the eastern cavity wall (*A1*) peaks at a slightly higher radial velocity ($-33.9 \pm 1.4 \text{ km s}^{-1}$) than the emission peak (*A2*) from the base of the northern cavity wall ($-16.9 \pm 1.5 \text{ km s}^{-1}$).
- We confirm the presence of a velocity gradient in the outflow cavity, transverse to the outflow axis, traced in H_2 . We generate a velocity centroid map to probe this observed velocity gradient. The magnitude of this velocity difference is $\sim 10 \text{ km s}^{-1}$ and exists between the northern and eastern pointing cavity walls, see Table 1. We discuss some possible explanations for the origin of this velocity gradient in Sect. 4.3. We rule out outflow rotation as the sole origin due to

large specific angular momenta values, $J(r) = 3217 \pm 658$ to $3867 \pm 1125 \text{ km s}^{-1} \text{ au}$ calculated from $1''$ to $2''$ offset from the central source. We instead favour a dissymmetry in the ambient material surrounding the outflow or the presence of multiple outflows.

- The morphology of the NIR continuum, H_2 1-0 S(1), $[\text{Fe II}] \lambda 2.047 \mu\text{m}$ and $\text{Br-}\gamma$ emission is presented. The continuum emission displays an approximately parabolic and asymmetric reflection nebula, that we interpret as a boundary region between the outflow and the ambient material, sweeping out a wide-angled cavity in the quiescent material. We recover a point source at the apex of this cavity which we establish as the source position. The H_2 emission displays a striking V-shaped morphology tracing the limb-brightened cavity walls of the outflow. We infer that the cavity structure we see has a 3-Dimensional inverted-conical shape, surrounding the atomic jet. The forging of this outflow cavity, which we determine to be an interaction region between the outflow and the surrounding quiescent material, may be due to some wide-angled wind, or expanding shells of material produced by and episodic wide-angled wind, or by the stacking of successive jet bowshocks from a collimated, variable inner jet propagating into a density-stratified surrounding medium. The morphological components labelled *A1*, *A2* and *A3* may arise due to multiple expanding shells, with a smaller scale shell, associated with the shocked emission peaks *A1* and *A2*, expanding within a slightly larger scale shell associated with the outer cavity walls produced by an earlier outburst of the wide-angled wind, or by a successive jet bowshock. The high-velocity $[\text{Fe II}]$ and $\text{Br-}\gamma$ emission traces the base of the atomic jet that culminates in a jet knot at approximately $1''.0$ or 450 au from the source position.
- We find radial stratification of the outflow in different emission tracers which produces an onion-like flow structure as discussed in Sect. 4.2. The slow-moving, wide-angled molecular outflow cavity traced in H_2 emission surrounds the base of the hotter, high-velocity atomic jet traced in $[\text{Fe II}]$ and $\text{Br-}\gamma$ emission. The H_2 outflow cavity lies within the reflection nebula seen in continuum emission, extending less laterally and having a narrower opening angle. The H_2 outflow cavity is also nested within the molecular outflow traced in ^{12}CO (2-1), and appears to curl inward towards the outflow axis at a distance along the outflow of approximately $4''$.
- The reflection nebula seen in continuum emission, the H_2 outflow cavity and, the atomic jet traced in $[\text{Fe II}]$ and $\text{Br-}\gamma$, are all asymmetric about the outflow direction. This is discussed in Sect. 4.2. We provide explanations for the origin of the H_2 outflow cavity asymmetries including density variations in the surrounding ambient material, and the influence of multiple outflows, it is plausible that both components of the binary source are driving outflows. We observe bending of the atomic jet, which emanates from the source position and tends towards the northern cavity wall, which is indicative of jet wiggling that we observe in this jet at larger scales.

This paper displays the wealth of information that can be extracted from IFU observations of protostellar outflows on intermediate scales in the NIR, and also highlights the morphological and kinematical complexity that needs to be considered when interpreting various aspects of outflows on these scales. In

particular, we want to emphasise that radial velocity gradients observed transverse to the outflow axis can be misinterpreted as rotation signatures, when other effects, as discussed, can produce equivalent transverse velocity gradients.

Acknowledgements. This work supported by the John & Pat Hume Doctoral Scholarship at Maynooth University (MU) and the Travelling Doctoral Studentship from the National University of Ireland (NUI).

References

- Agra-Amboage, V., Cabrit, S., Dougados, C., et al. 2014, *A&A*, 564, A11
- Anderson, J. M., Li, Z.-Y., Krasnopolsky, R., & Blandford, R. D. 2003, *ApJ*, 590, L107
- Antonucci, S., Nisini, B., Giannini, T., & Lorenzetti, D. 2008, *A&A*, 479, 503
- Arce, H. G., Mardones, D., Corder, S. A., et al. 2013, *ApJ*, 774, 39
- Arce, H. G., Shepherd, D., Gueth, F., et al. 2007, in *Protostars and Planets V*, ed. B. Reipurth, D. Jewitt, & K. Keil, 245
- Bai, X.-N., Ye, J., Goodman, J., & Yuan, F. 2016, *ApJ*, 818, 152
- Belloche, A. 2013, in *EAS Publications Series*, Vol. 62, *EAS Publications Series*, ed. P. Hennebelle & C. Charbonnel, 25–66
- Beuther, H., van Dishoeck, E. F., Tychoniec, L., et al. 2023, *Astronomy & Astrophysics*, 673, A121
- Bjerkeli, P., van der Wiel, M. H. D., Harsono, D., Ramsey, J. P., & Jørgensen, J. K. 2016, *Nature*, 540, 406
- Bonnefoy, M., Chauvin, G., Lagrange, A.-M., et al. 2014, *Astronomy & Astrophysics*, 562, A127
- Cabrit, S., Pety, J., Pesenti, N., & Dougados, C. 2006, *A&A*, 452, 897
- Caratti o Garatti, A., Giannini, T., Nisini, B., & Lorenzetti, D. 2006, *A&A*, 449, 1077
- Coffey, D. 2017, *Nature Astronomy*, 1, 0180
- Coffey, D., Bacciotti, F., Ray, T. P., Eisloffel, J., & Woitas, J. 2007, *ApJ*, 663, 350
- Coffey, D., Bacciotti, F., Woitas, J., Ray, T. P., & Eisloffel, J. 2004, *ApJ*, 604, 758
- Davis, C. J. 2002, in *Revista Mexicana de Astronomia y Astrofisica Conference Series*, Vol. 13, *Revista Mexicana de Astronomia y Astrofisica Conference Series*, ed. W. J. Henney, W. Steffen, L. Binette, & A. Raga, 36–42
- Davis, C. J., Cervantes, B., Nisini, B., et al. 2011, *A&A*, 528, A3
- Davis, C. J., Whelan, E., Ray, T. P., & Chrysostomou, A. 2003, *A&A*, 397, 693
- De Colle, F., Cerqueira, A. H., & Riera, A. 2016, *ApJ*, 832, 152
- de Valon, A., Dougados, C., Cabrit, S., et al. 2022, *A&A*, 668, A78
- Delabrosse, V., Dougados, C., Cabrit, S., et al. 2024, *arXiv e-prints*, arXiv:2403.19400
- Demars, D., Bonnefoy, M., Dougados, C., et al. 2023, *A&A*, 676, A123
- Eisenhauer, F., Abuter, R., Bickert, K., et al. 2003, in *Society of Photo-Optical Instrumentation Engineers (SPIE) Conference Series*, Vol. 4841, *Instrument Design and Performance for Optical/Infrared Ground-based Telescopes*, ed. M. Iye & A. F. M. Moorwood, 1548–1561
- Eisloffel, J. & Mundt, R. 1994, *A&A*, 284, 530
- Erkal, J., Dougados, C., Coffey, D., et al. 2021a, *A&A*, 650, A46
- Erkal, J., Nisini, B., Coffey, D., et al. 2021b, *ApJ*, 919, 23
- Ferreira, J. 1997, *A&A*, 319, 340
- Ferreira, J., Dougados, C., & Cabrit, S. 2006, *A&A*, 453, 785
- Frank, A., Ray, T. P., Cabrit, S., et al. 2014, in *Protostars and Planets VI*, ed. H. Beuther, R. S. Klessen, C. P. Dullemond, & T. Henning, 451–474
- Freudling, W., Romaniello, M., Bramich, D. M., et al. 2013, *A&A*, 559, A96
- García Lopez, R., Nisini, B., Eisloffel, J., et al. 2010, *A&A*, 511, A5
- Gaudel, M., Maury, A. J., Belloche, A., et al. 2020, *A&A*, 637, A92
- Graham, J. A. & Heyer, M. H. 1989, *PASP*, 101, 573
- Habel, N. M., Megeath, S. T., Booker, J. J., et al. 2021, *ApJ*, 911, 153
- Harsono, D., Bjerkeli, P., Ramsey, J., et al. 2023, *The Astrophysical Journal Letters*, 951, L32
- Hartigan, P. 2003, *Jets in Young Stellar Objects: Theory and Observations*, 111
- Hartigan, P., Frank, A., Foster, J. M., et al. 2011, *ApJ*, 736, 29
- Hartigan, P., Heathcote, S., Morse, J. A., Reipurth, B., & Bally, J. 2005, *AJ*, 130, 2197
- Heathcote, S., Morse, J. A., Hartigan, P., et al. 1996, *AJ*, 112, 1141
- Jones, A., Noll, S., Kausch, W., Szyszka, C., & Kimeswenger, S. 2013, *A&A*, 560, A91
- Konigl, A. & Pudritz, R. E. 2000, in *Protostars and Planets IV*, ed. V. Mannings, A. P. Boss, & S. S. Russell, 759
- Launhardt, R., Pavlyuchenkov, Y. N., Akimkin, V. V., et al. 2023, *A&A*, 678, A135
- Lee, C.-F., Ho, P. T. P., Li, Z.-Y., et al. 2017, *Nature Astronomy*, 1, 0152
- Lee, C.-F., Mundy, L. G., Reipurth, B., Ostriker, E. C., & Stone, J. M. 2000, *ApJ*, 542, 925
- Lee, C.-F., Tabone, B., Cabrit, S., et al. 2021, *ApJ*, 907, L41
- Li, Z.-Y. & Shu, F. H. 1996, *ApJ*, 468, 261
- López-Vázquez, J. A., Lee, C.-F., Fernández-López, M., et al. 2024, *ApJ*, 962, 28
- Louvet, F., Dougados, C., Cabrit, S., et al. 2016, *A&A*, 596, A88
- Louvet, F., Dougados, C., Cabrit, S., et al. 2018, *A&A*, 618, A120
- Palma-Bifani, P., Chauvin, G., Bonnefoy, M., et al. 2023, *A&A*, 670, A90
- Panoglou, D., Cabrit, S., Pineau Des Forêts, G., et al. 2012, *A&A*, 538, A2
- Pascucci, I., Cabrit, S., Edwards, S., et al. 2023, in *Astronomical Society of the Pacific Conference Series*, Vol. 534, *Protostars and Planets VII*, ed. S. Inutsuka, Y. Aikawa, T. Muto, K. Tomida, & M. Tamura, 567
- Petrus, S., Bonnefoy, M., Chauvin, G., et al. 2021, *A&A*, 648, A59
- Pudritz, R. E. & Norman, C. A. 1983, *ApJ*, 274, 677
- Pudritz, R. E., Ouyed, R., Fendt, C., & Brandenburg, A. 2007, in *Protostars and Planets V*, ed. B. Reipurth, D. Jewitt, & K. Keil, 277
- Pudritz, R. E. & Ray, T. P. 2019, *Frontiers in Astronomy and Space Sciences*, 6, 54
- Rabananahary, M., Cabrit, S., Meliani, Z., & Pineau des Forêts, G. 2022, *A&A*, 664, A118
- Ray, T. P. & Ferreira, J. 2021, *New A Rev.*, 93, 101615
- Ray, T. P., McCaughrean, M. J., Caratti o Garatti, A., et al. 2023, *Nature*, 622, 48
- Reipurth, B., Yu, K. C., Heathcote, S., Bally, J., & Rodríguez, L. F. 2000, *AJ*, 120, 1449
- Richer, J. S., Shepherd, D. S., Cabrit, S., Bachiller, R., & Churchwell, E. 2000, in *Protostars and Planets IV*, ed. V. Mannings, A. P. Boss, & S. S. Russell, 867
- Schwartz, R. D. 1977, *Astrophysical Journal, Lett.*, Vol. 212, p. L25-L26, 212, L25
- Schwartz, R. D. 1983, *ApJ*, 268, L37
- Shang, H., Krasnopolsky, R., Liu, C.-F., & Wang, L.-Y. 2020, *ApJ*, 905, 116
- Shu, F. H., Najita, J. R., Shang, H., & Li, Z. Y. 2000, in *Protostars and Planets IV*, ed. V. Mannings, A. P. Boss, & S. S. Russell, 789–814
- Skrutskie, M. F., Cutri, R. M., Stiening, R., et al. 2006, *AJ*, 131, 1163
- Soker, N., Bublitz, J., & Kastner, J. H. 2022, *ApJ*, 928, 159
- Staff, J., Koning, N., Ouyed, R., Thompson, A., & Pudritz, R. 2014, *arXiv preprint arXiv:1411.3440*
- Stanke, T., McCaughrean, M. J., & Zinnecker, H. 1999, *A&A*, 350, L43
- Tabone, B., Cabrit, S., Bianchi, E., et al. 2017, *A&A*, 607, L6
- Tsakamoto, Y., Maury, A., Commerçon, B., et al. 2023, in *Astronomical Society of the Pacific Conference Series*, Vol. 534, *Protostars and Planets VII*, ed. S. Inutsuka, Y. Aikawa, T. Muto, K. Tomida, & M. Tamura, 317
- van Kempen, T. A., van Dishoeck, E. F., Güsten, R., et al. 2009, *A&A*, 501, 633
- Wang, L., Bai, X.-N., & Goodman, J. 2019, *The Astrophysical Journal*, 874, 90
- Whelan, E. & Garcia, P. 2008, *Jets from Young Stars II: Clues from High Angular Resolution Observations*, 123
- Whelan, E. T. 2014, *Astronomische Nachrichten*, 335, 537
- Wilking, B. A., Schwartz, R. D., Mundy, L. G., & Schultz, A. S. B. 1990, *AJ*, 99, 344
- Yang, Y.-L., Green, J. D., Pontoppidan, K. M., et al. 2022, *The Astrophysical Journal Letters*, 941, L13
- Zhang, Y., Arce, H. G., Mardones, D., et al. 2016, *ApJ*, 832, 158
- Zhang, Y., Arce, H. G., Mardones, D., et al. 2019, *ApJ*, 883, 1
- Zhang, Y., Higuchi, A. E., Sakai, N., et al. 2018, *ApJ*, 864, 76
- Zhu, Z. & Stone, J. M. 2018, *ApJ*, 857, 34

Appendix A: OH wavelength calibration map

Figure A.1 illustrates the effect of the OH line wavelength recalibration on the H₂ emission velocity centroid maps. The magnitude of the wavelength/velocity correction, shown in the central panel, varies between ~ -26 km s⁻¹ and -30 km s⁻¹ and varies most significantly in the vertical direction. This wavelength correction map was applied to the SINFONI datacube around the H₂ 1–0 S(1) emission line at 2.12 μ m, effectively obtaining a more accurate wavelength calibration than that offered with the standard arc lamp wavelength calibration.

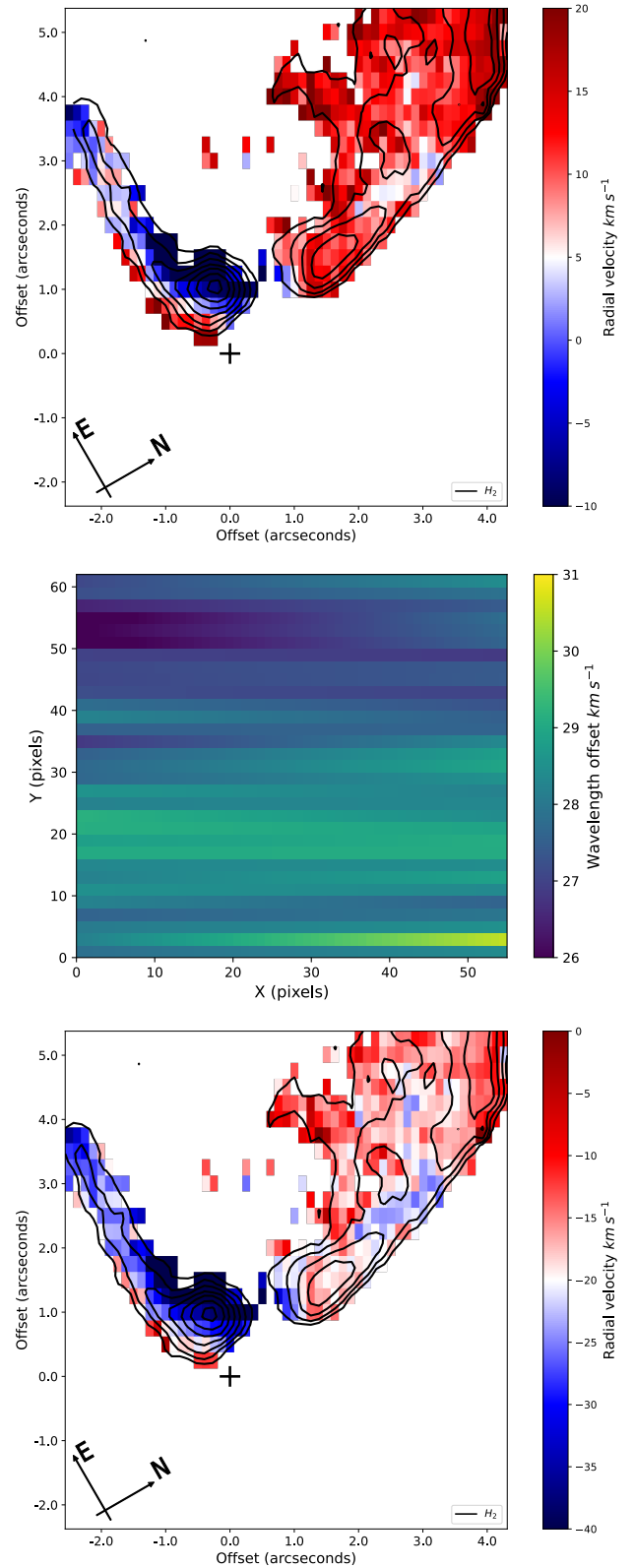


Fig. A.1. Velocity centroid maps of H₂ emission before (*top*), and after (*bottom*), the wavelength recalibration map (*centre*), derived from the OH emission lines, is applied. Notice the change in velocity scales used for the velocity centroid maps. The source position is represented with a black plus symbol in the velocity centroid maps. Contour levels for both begin at 3σ of the background emission and increase by factors of 1.5.

Appendix B: Uneven slit effect correction

In order to correct for uneven slit illumination, we follow the method outlined in (Agra-Amboage et al. 2014; Erkal et al. 2021a). First, we model the distribution of incoming light by spectrally integrating the emission line of interest and the local continuum emission either side of the emission line. We then estimate the brightness centroid and its displacement with respect to the centre of the slitlet at each spaxel in the datacube. The spurious wavelength shift, expressed in terms of a velocity shift, is calculated using the adapted formula, derived by Marconi et al. (2003), shown below:

$$\Delta v(x_0, y_0) = \frac{\delta u}{\delta y} \times \frac{\iint I_{\text{mod}}(u, v) \times (v - y_0) du dv}{\iint I_{\text{mod}}(u, v) du dv} \quad (\text{B.1})$$

Here, δu is the spectral pixel sampling, δy is the width of the slitlet, and I_{mod} is the modelled light intensity integrated over a single spaxel of detector coordinates (x_0, y_0) . Figure B.1 displays the 2D wavelength correction map computed around the H₂ $\lambda 2.122 \mu\text{m}$ emission line. Velocity corrections here vary from -5 km s^{-1} to $+10 \text{ km s}^{-1}$. As expected, the velocity corrections have a strong variation in the vertical, or dispersion direction due to the nature of the horizontal slicing mirrors present in the SINFONI instrument. The effect due to uneven slit illumination is more prominent in brighter emission and more compact emission.

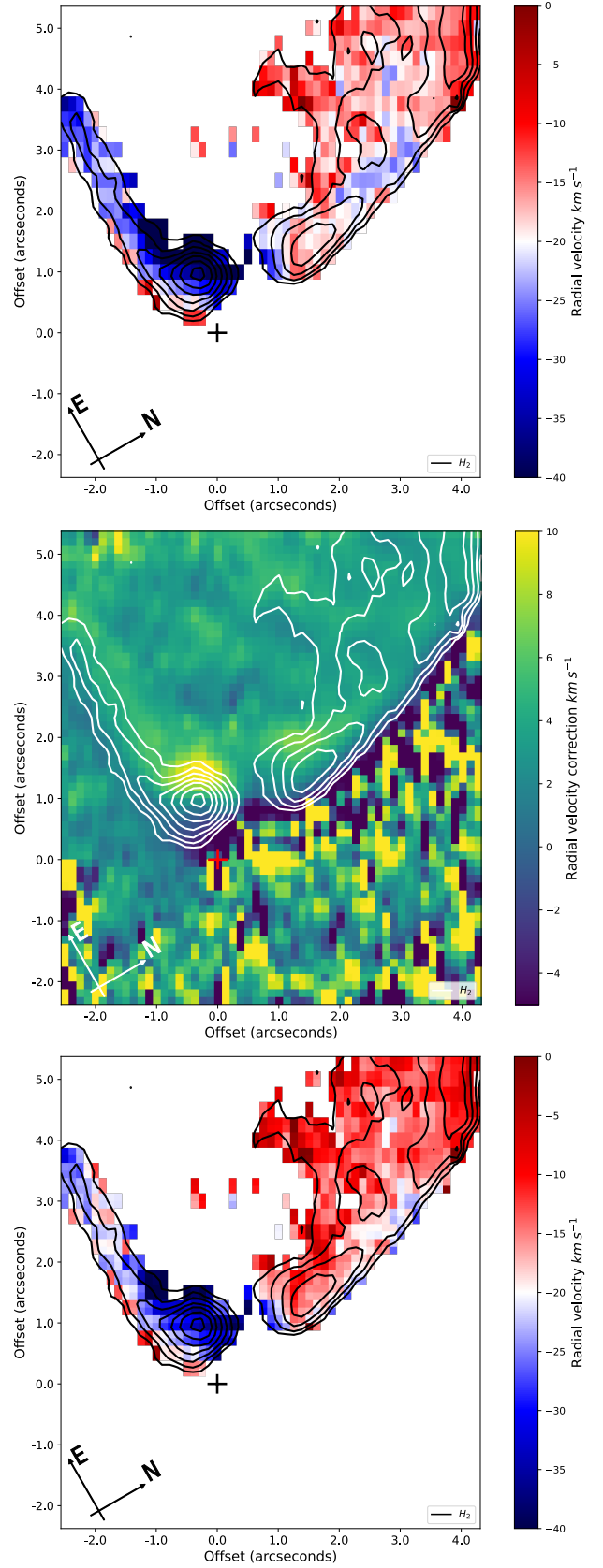


Fig. B.1. Velocity centroid maps of H₂ emission before (*top*), and after (*bottom*), the wavelength correction map required to amend illusory wavelength/velocity shifts due to uneven slit illumination (*centre*), is applied. In the central figure H₂ emission is overplotted in white contours. The continuum peak position is marked with a red plus symbol. Contour levels for the 3 panels begin at 3σ of the background emission and increase by factors of 1.5.

Appendix C: Effect of scattered emission removal

Figure C.1 displays the integrated H₂ 1-0 S(1) line emission before (*top*), and after (*bottom*), the scattered emission removal routine is performed. It is clear that after the scattered light is subtracted, there is a steeper intensity gradient associated with the intrinsic H₂ emission, which is most readily observable in the closeness of contour lines surrounding bright H₂ emission, such as the features labelled A1 & A2. Nebulous emission close the apex of the cavity has also been diminished after scattered light subtraction. The bottom panel also displays, with a red rectangular region, the position and width of the pseudo-slit used to extract the transverse PV diagram seen in Fig. 5.

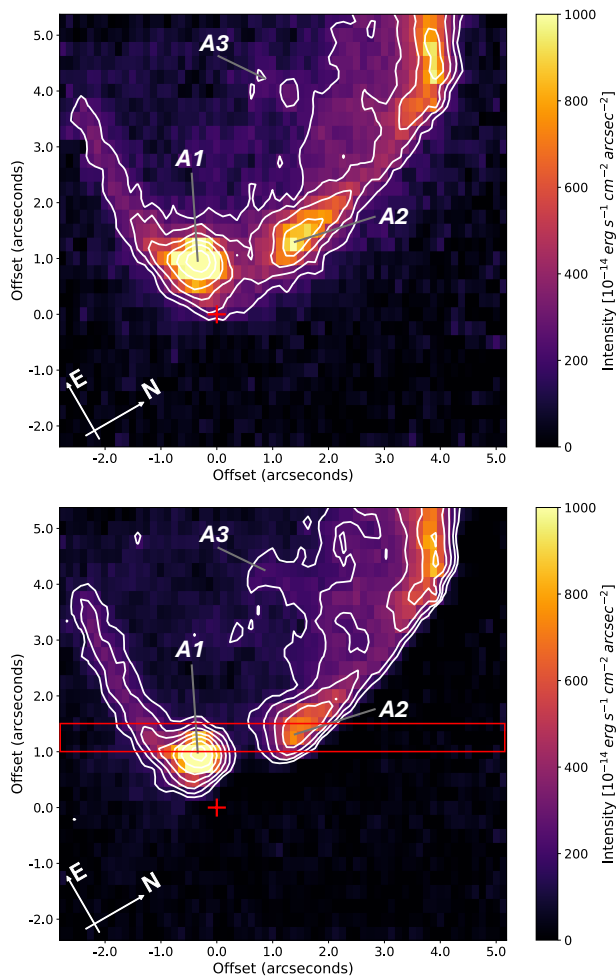


Fig. C.1. Figure displaying integrated H₂ line emission before (*top*) and after (*bottom*) the scattered emission removal routine is performed. The source position is represented with a red plus symbol. Contour levels for both begin at 3σ of the background emission and increase by factors of 1.5. The red rectangle in the bottom panel displays the position and width of the pseudo-slit used to extract the transverse PV diagram seen in Fig. 5.

Appendix D: Supplementary spectra

Figure D.1 displays three integrated spectra extracted from various spatial positions on the object. Molecular hydrogen emission lines (H₂), forbidden iron emission ([Fe II]), Br- γ emission and CO emission are common to all spectra.

The top spectrum in Fig. D.1 was extracted using a circular aperture of radius 0.''4 from the atomic jet knot located approxi-

mately 450 au, or 1.''0, from the source position. This knot allows us to study the jet close to the base of the outflow. Atomic forbidden emission lines are identified in this spectrum tracing the collimated jet emanating from the source. Br- γ is also identified here with a double peaked structure displaying strong emission in the blueshifted peak. This implies that Br- γ here is tracing not only accretion processes onto the star but also ejection, namely the base of the atomic jet. Molecular hydrogen (H₂) emission lines also tracing the outflow are identified.

The central spectrum in Fig. D.1 displays a spectrum extracted using a circular aperture of radius 0.''4 from the H₂ knot labelled A1 on the left side of the limb-brightened V-shaped cavity traced by molecular hydrogen. The H₂ emission lines here are very bright. Comparatively, the spectrum in the bottom of Fig. D.1 extracted using a circular aperture of radius 0.''4, but from the H₂ knot labelled A2 on the right side of the V-shaped cavity traced by molecular hydrogen. The H₂ emission lines here are not as strong as they appear on the left side of the V-shaped cavity. This is expected as the left knot of the cavity has a significantly greater intensity when compared with the knot on the right side.

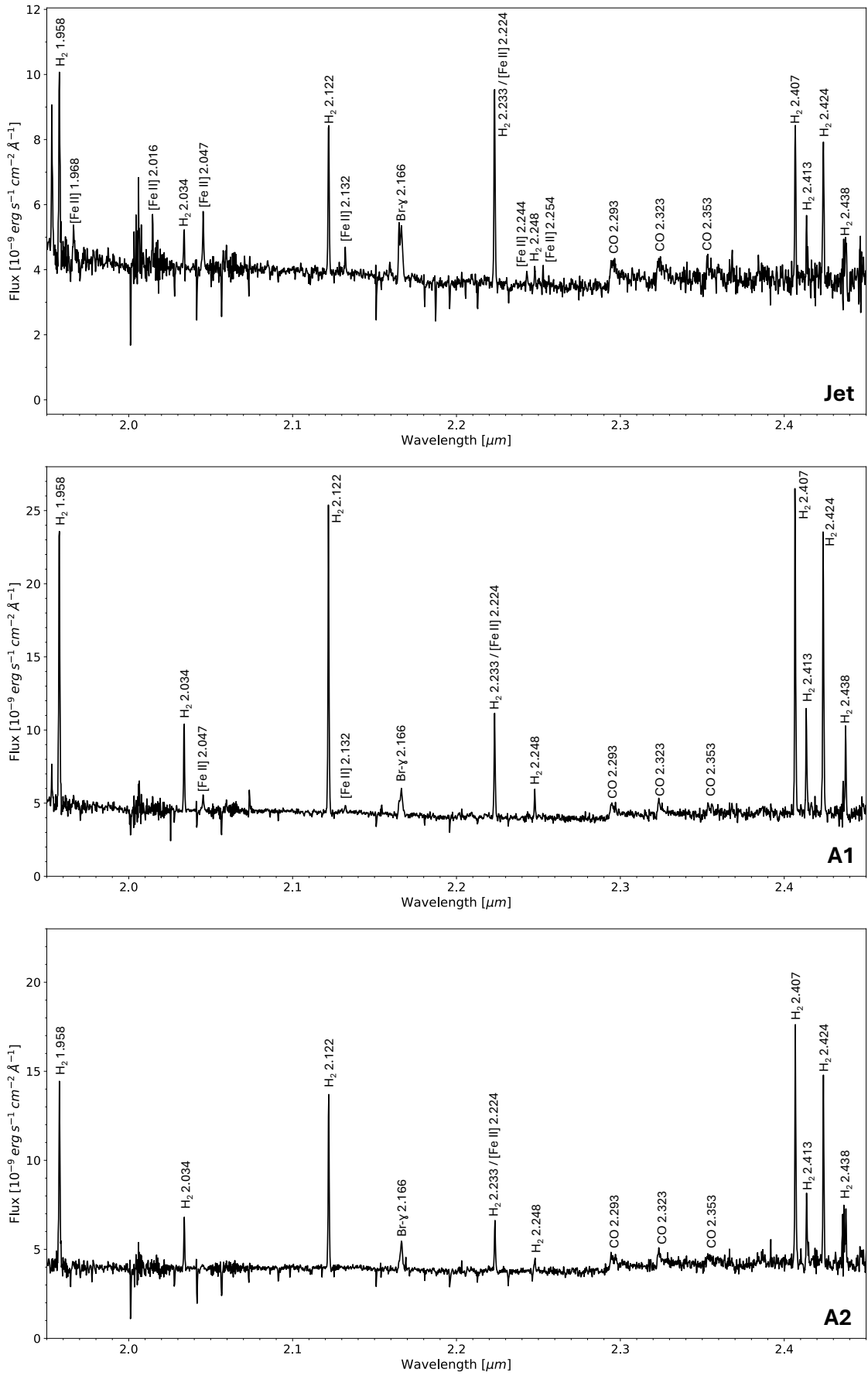


Fig. D.1. *Top:* Integrated spectrum extracted using a circular aperture of radius $0''.4$ from atomic jet knot located at $1''$ offset from source position. *Centre:* Integrated spectrum extracted using a circular aperture of radius $0''.4$ from base of left cavity wall traced in H_2 , position A1. *Bottom:* Integrated spectrum extracted using a circular aperture of radius $0''.4$ from base of cavity wall, position A2.